

Heat Transport across Dissimilar Materials

Nitin Chandra Shukla

Dissertation submitted to the faculty of the Virginia Polytechnic Institute and State University in partial fulfillment of the requirements for the degree of

Doctor of Philosophy
In
Mechanical Engineering

Professor Scott T. Huxtable, Committee Chair
Professor Thomas E. Diller
Professor Kathleen Meehan
Professor Giti Khodaparast
Professor Mark R. Paul

May 13, 2009
Blacksburg, VA

Keywords: Nanoscale heat transport, thermal conductivity, interface thermal conductance, nanocomposite, metallic glass, time-domain thermoreflectance

Copyright (2009)

Heat Transport across Dissimilar Materials

Nitin Chandra Shukla

Abstract

All interfaces offer resistance to heat transport. As the size of a device or structure approaches nanometer lengthscales, the contribution of the interface thermal resistance often becomes comparable to the intrinsic thermal resistance offered by the device or structure itself. In many microelectronic devices, heat has to transfer across a metal-nonmetal interface, and a better understanding about the origins of this interface thermal conductance (inverse of the interface thermal resistance) is critical in improving the performance of these devices. In this dissertation, heat transport across different metal-nonmetal interfaces are investigated with the primary goal of gaining qualitative and quantitative insight into the heat transport mechanisms across such interfaces. A time-domain thermoreflectance (TDTR) system is used to measure the thermal properties at the nanoscale. TDTR is an optical pump-probe technique, and it is capable of measuring thermal conductivity, k , and interface thermal conductance, G , simultaneously.

The first study examines k and G for amorphous and crystalline $Zr_{47}Cu_{31}Al_{13}Ni_9$ metallic alloys that are in contact with poly-crystalline Y_2O_3 . The motivation behind this study is to determine the relative importance of energy coupling mechanisms such as electron-phonon or phonon-phonon coupling across the interface by changing the material structure (from amorphous to crystalline), but not the composition. From the TDTR measurements $k=4.5 \text{ W m}^{-1} \text{ K}^{-1}$ for the amorphous metallic glass of

$Zr_{47}Cu_{31}Al_{13}Ni_9$, and $k=5.0 \text{ W m}^{-1} \text{ K}^{-1}$ for the crystalline $Zr_{47}Cu_{31}Al_{13}Ni_9$. TDTR also gives $G=23 \text{ MW m}^{-2} \text{ K}^{-1}$ for the metallic glass/ Y_2O_3 interface and $G=26 \text{ MW m}^{-2} \text{ K}^{-1}$ for the interface between the crystalline $Zr_{47}Cu_{31}Al_{13}Ni_9$ and Y_2O_3 . The thermal conductivity of the poly-crystalline Y_2O_3 layer is found to be $k=5.0 \text{ W m}^{-1} \text{ K}^{-1}$. Despite the small difference between k and G for the two alloys, the results are repeatable and they indicate that the structure of the alloy plays a role in the electron-phonon coupling and interface conductance.

The second experimental study examines the effect of nickel nanoparticle size on the thermal transport in multilayer nanocomposites. These nanocomposites consist of five alternating layers of nickel nanoparticles and yttria stabilized zirconia (YSZ) spacer layers that are grown with pulsed laser deposition. Using TDTR, thermal conductivities of $k=1.8, 2.4, 2.3,$ and $3.0 \text{ W m}^{-1} \text{ K}^{-1}$ are found for nanocomposites with nickel nanoparticle diameters of 7, 21, 24, and 38 nm, respectively, and $k=2.5 \text{ W m}^{-1} \text{ K}^{-1}$ for a single 80 nm thick layer of YSZ. The results indicate that the overall thermal conductivity of these nanocomposites is strongly influenced by the Ni nanoparticle size and the interface thermal conductance between the Ni particles and the YSZ matrix. An effective medium theory is used to estimate the lower limits for the interface thermal conductance between the nickel nanoparticles and the YSZ matrix ($G>170 \text{ MW m}^{-2} \text{ K}^{-1}$), and the nickel nanoparticle thermal conductivity.

Acknowledgements

During the course of my Ph.D., I feel fortunate to have known so many nice and lovely people at Virginia Tech. First, I would like to acknowledge my advisor Dr. Scott Huxtable for his support, inspiration and encouragement throughout my Ph.D. I am grateful to him for his invaluable advising and for providing me with so many opportunities to learn new things.

I am thankful to Dr. Giti Khodaparast for allowing me to work in her laser lab. Talking to her was always inspiring, and I really appreciate her helpful comments on my research work. I would also like to thank my other committee members Dr. Thomas Diller, Dr. Kathleen Meehan, and Dr. Mark Paul for serving on my committee and for giving me good direction and advice on my research.

I also thank Dr. Jeremiah Abiade and Dr. Peter Liaw for providing me with samples that were crucial to my research work. I greatly appreciate the assistance of Dr. W. T. Reynolds, Jr., Dr. M. Murayama, and J. McIntosh with structural characterizations of my samples.

I would also like to thank Hao-Hsiang Liao who is a great friend in addition to being a labmate. I will always remember our passionate yet funny discussions on the Red Sox-Yankees rivalry while working late at night or over the weekends. I would also like to acknowledge the assistance and efforts offered by my labmates Harikrishna, Chris Vernieri, Matthew Cobert, Brooks Mann, Rebekah Derryberry, and Leron Vandsburger. I also appreciate Don Leber, Rajeev Kini, Matthew Frazier, Krishna Vummidi, Ali Hajjiah,

Joe Wood, and Russel Mammei for sharing their knowledge and helping me with the laser and cleanroom work.

I would like to thank my friends who always encouraged me and were very supportive of my Ph.D.: Owais Farooqi, Ashvin Mudaliar, Leepika Tuli, Bhawani Kasula, Ritesh Agarwal, Ramesh Singh, Gaurav Singh, Apoorva Shende, and Saurabh Bisht.

Finally, I wish to acknowledge my family who is always there to support me. I will always be indebted to my parents for their unconditional love and care, and for teaching me all the good values in life. I would also thank Richa for her support and patience.

Dedication

*To my parents
who are my constant inspiration.*

Table of Contents

Abstract.....	ii
Acknowledgements.....	iv
Dedication.....	vi
Table of Contents.....	vii
List of Figures.....	x
List of Tables.....	xii
Nomenclature.....	xiii
1. Introduction.....	1
1.1. Basic philosophy of heat transport.....	1
1.2. Effect of lengthscale on heat transport.....	3
1.2.1. Macro lengthscales of approximate sizes of one micrometer and above.....	3
1.2.2. Nanoscale lengthscales of approximate sizes of one micrometer and less.....	4
1.3. Motivation.....	6
1.4. Objective.....	8
1.4.1. Scope of work.....	9
2. Background.....	11
2.1. Crystal vibrations.....	11
2.2. Phonons.....	14
2.3. Phonon scattering.....	16
2.3.1. Scattering by crystal imperfections.....	17
2.3.2. Inelastic scattering.....	18
2.4. Temperature dependence of phonon scattering.....	20

2.5. Heat transport in low-dimensional structures	22
2.6. Interface thermal conductance	23
2.6.1. Acoustic Mismatch Model (AMM)	25
2.6.2. Diffuse Mismatch Model	27
2.6.3. Phonon radiation limit.....	29
2.7. Literature survey on interface thermal conductance.....	29
3. Experiments	39
3.1. 3- ω Method	39
3.2. Time Domain Thermo-Reflectance (TDTR) technique.....	43
3.2.1. Experimental setup.....	47
3.2.2 Verification of the TDTR setup	55
4. Thermal conductivity and interface thermal conductance of amorphous and crystalline Zr ₄₇ Cu ₃₁ Al ₁₃ Ni ₉ alloys with a Y ₂ O ₃ coating.....	58
4.1. Abstract	58
4.2. Introduction.....	58
4.3. Sample Preparation	60
4.4. Results.....	61
5. Thermal transport in composites of self-assembled nickel nanoparticles embedded in yttria stabilized zirconia.....	69
5.1. Abstract	69
5.2. Introduction.....	69
5.3. Sample preparation	70
5.4. Results.....	72

6. Conclusions and Future Work	80
6.1. Future directions	82
Appendix A.....	84
Bibliography	92

List of Figures

Figure 1: Energy-distance plot for an atom in a lattice.....	12
Figure 2: A spring-mass system.....	12
Figure 3: Phonon dispersion relation.....	14
Figure 4: Quantum-mechanical oscillator.....	15
Figure 5: Phonon-phonon scattering.....	20
Figure 6: Temperature dependence of lattice thermal conductivity of solids.....	22
Figure 7: Scattering of a phonon at the interface.....	26
Figure 8: Plot of ratio of interface thermal conductances predicted by DMM and AMM, respectively, as a function of the amount of mismatch.....	28
Figure 9: Two pathways for heat carrier coupling at a metal/nonmetal interface.	34
Figure 10: Summary of experimental data taken for the interface thermal conductance for various solid-solid interfaces with temperature.....	38
Figure 11: 3ω method for measuring thermal conductivity of thin films and bulk solids.....	40
Figure 12: Temperature measurement of thermal conductivity for a Pyrex sample.....	43
Figure 13: Time-domain thermoreflectance (TDTR) setup.....	52
Figure 14: The electronics associated with the modulation of the pump beam and the measurement of thermoreflectance signal using a RF lock-in amplifier.	53
Figure 15: Use of optical filters for efficient rejection of reflected pump.....	54
Figure 16: TDTR LabVIEW program.....	55
Figure 17: TDTR signal for PECVD oxide, fused quartz, and sapphire samples.	57

Figure 18: Transmission electron micrographs of (a) crystalline $Zr_{47}Cu_{31}Al_{13}Ni_9$ with Y_2O_3 and Al, and (b) amorphous $Zr_{47}Cu_{31}Al_{13}Ni_9$ with Y_2O_3 and Al. 63

Figure 19: X-ray diffraction (XRD) patterns for Y_2O_3 , amorphous and crystalline $Zr_{47}Cu_{31}Al_{13}Ni_9$ alloys, and Si. 64

Figure 20: Time-domain thermoreflectance data (TDTR) on the Al/ Y_2O_3 /alloys and the Al/ Y_2O_3 /Si sample. 65

Figure 21: Schematic diagram of the Van der Pauw method for an arbitrarily shaped flat structure. 66

Figure 22: Scanning transmission electron micrographs of the Ni/YSZ nanocomposites. 71

Figure 23: TDTR modeling for each period of nanocomposite. Each period consists of the YSZ spacer and Ni nanoparticle layers. 73

Figure 24: Interface thermal conductance between the Ni nanoparticles and the surrounding YSZ matrix as a function of Ni nanoparticle thermal conductivity. 79

List of Tables

Table 1: Summary of typical properties of electron and phonons	6
Table 2: The dominant wavelength of phonons in solids	24
Table 3. Measured interface thermal conductance for metal-dielectric interfaces at room temperature [47]. The temperature in parenthesis represents the Debye temperature of the material.	31
Table 4: Compilation of measured interface thermal conductance of important solid-solid interfaces.....	36
Table 5: Summary of properties for each sample. The effective thermal conductivity of the Ni/YSZ composite layers is extracted with TDTR. The overall thermal conductivity of the nanocomposite is calculated using a series thermal model in conjunction with our measurements on YSZ and the Ni/YSZ composite layers.....	75

Nomenclature

C	Heat Capacity
E	Energy
f	Frequency
G	Interface Thermal Conductance
h	Planck's Constant
\hbar	Planck's Constant divide by 2π
k	Thermal Conductivity
K	Wave Number
k_B	Boltzmann Constant
p	Momentum
q''	Heat Flux
t	Time
T	Temperature
v	Speed
λ	Wavelength
ω	Angular Frequency

1. Introduction

1.1. Basic philosophy of heat transport

The concept of energy is as old as the age of this universe. The Big Bang explosion gave birth to this universe releasing matter and energy and creating the time-space fabric. Every phenomenon in this universe starting from the birth of a star to the evolution of life is a direct or indirect result of interactions between matter and energy. The energy transport in matter, space and time domains describe all the events that occur in this world. As an *intelligent* life-form who is eager to unravel the truths about our universe, it is of paramount interest to us to understand the transport of energy at all length and time scales.

As we all know, matter in its elementary form can be assumed to be composed of atoms. The atoms and molecules interact through interatomic attractive forces, and the magnitude of these forces decides the state of matter. In the solid state, atoms are bound together by strong chemical bonds, and the relative positions of atoms are fixed in the absence of external forces. Liquids and gases have no such fixed atomic arrangement and cannot sustain shear stress. In liquids, the atoms are bound together by weak van der Waals forces and have a small degree of cohesion. In gases, the chemical attraction force among atoms is negligible. Therefore, the atoms in a gas move in an irregular manner and collide randomly with each other.

The temperature, T , of matter is related to the average kinetic energy of particles. The energy associated with temperature is defined as heat. As energy or heat is supplied to solids, atoms start vibrating around their equilibrium positions. If the energy supplied

is less than the chemical potential energy, then atoms are set in an oscillatory motion about their equilibrium position, giving rise to a thermal wave known as phonon. A phonon is a quantized lattice vibration, and it transports energy as it moves. If the energy transferred is more than the chemical potential energy of the solid, the amplitude of the oscillation will become so high that the chemical bonds will be broken and the solid will convert into a liquid or gas. It is interesting to note that as liquids and gases do not have regular periodic atomic structures, they cannot sustain long-range order phonons. Therefore, the bulk of heat conduction in liquids and gases is through random collisions of excited atoms.

The scope of this dissertation includes heat transport in solids and between solid-solid interfaces. It is to be kept in mind that the term ‘transport’ means flow of mass, charge or heat [1]. Transport phenomenon describes processes that bring a system from a non-equilibrium state to an equilibrium state or vice versa. Heat transport is a process where the flow has established as a result of a thermal gradient.

Heat transport in solids is primarily controlled by electrical carriers (electrons and holes) and lattice vibrations (phonons), and to a lesser extent, electromagnetic waves, spin waves, and other types of excitations. In metals, heat transport is dominated by electrons due to the presence of a large number of free electrical carriers. In nonmetals, heat transport is mainly due to the phonons as there are not many free electrical carriers present in nonmetals.

The thermal conductivity, k , of a material is defined as the amount of heat transported per unit time, through a unit thickness, per unit area normal to heat flow to maintain a unit temperature difference. In simpler words, it is the ability of a material to

conduct heat. The overall, or total, thermal conductivity of a material can be defined as the sum of the thermal conductivities due to each excitation. In solids, the electrical carriers and phonons are the major contributors to thermal conductivity such that the overall thermal conductivity may be defined as: $k = k_{\text{electrical}} + k_{\text{phonon}}$, where $k_{\text{electrical}}$ and k_{phonon} are the electron and lattice components of thermal conductivity, respectively.

1.2. Effect of lengthscale on heat transport

There are two distinct lengthscale regimes that have to be kept in mind when studying heat transfer in solids:

1.2.1. Macro lengthscales of approximate sizes of one micrometer and above.

Heat transport in the macroscale regime has been studied extensively [2-4]. In this regime, phenomenological models such as constitutive relations are used rather than investigating the specific mechanisms of the energy transport. These models do not depend on either the energy transport mechanisms or the microstructure of the solid; instead they depend on bulk material properties such as thermal conductivity, density, and heat capacity.

At the microscale and above, temperature is well defined at every point in the region, and heat transfer is governed by Fourier's law of heat conduction:

$$q_x'' = -k(dT/dx) \quad (1.1)$$

where q_x'' is the heat flux along some direction x , k is the thermal conductivity of the material along the direction x , and dT is the temperature difference over a distance dx of the solid along the direction x . By combining the energy balance and Fourier's equation, we obtain the following relation:

$$k = \frac{1}{3} \sum_{\alpha} C_{\alpha} v_{\alpha} l_{\alpha} \quad (1.2)$$

where C is the total heat capacity, v is the average mean velocity of the heat carrier, and l is the mean free path of the energy carrier, and α is a summation over all of the heat carriers, i.e. electrons, phonons, etc. The mean free path is defined as the average distance between successive collisions for an energy carrier. The equation (1.2) is useful in predicting the temperature dependence of thermal conductivity.

1.2.2. Nanoscale lengthscales of approximate sizes of one micrometer and less.

As the device or structure size approaches the nanoscale, various scattering phenomena such as boundary scattering and interface scattering tend to become increasingly important in determining the overall heat transport. The important characteristic lengths of major energy carriers in solids are the mean free path (l) and the wavelength (λ) [5]. Typical values for l , λ , relaxation time, and the propagation speed for electrons and phonons are listed in Table 1 [6]. The relaxation time is defined as the time taken by the energy particle to attain local thermodynamic equilibrium.

For macroscale structures, it is evident from Table 1 that these energy carriers have adequate space to travel and attain equilibrium in time. On the other hand, for nanoscale structures, the size becomes comparable to the mean free path and wavelength of the heat carriers and the definition of temperature becomes questionable. Boundary scattering effects become dominant for such low dimensional structures and thermal conductivity is usually smaller than that of the bulk material [7, 8].

Interfaces also play a key role in nanoscale heat transport. Kapitza [1] first discovered the presence of interfacial thermal resistance between solid copper and

supercooled helium. The interface thermal resistance or Kapitza resistance, R , is defined by following relation:

$$R = \frac{\Delta T_{\text{int}}}{q''} \quad (1.3)$$

where ΔT_{int} is the observed temperature difference across the interface when a heat flux q'' is applied across the interface. The interface thermal conductance, G , is defined as $q'' = G\Delta T_{\text{int}}$, or the inverse of interface boundary resistance.

For most solid-solid interfaces, G spans a range of 8 to 300 MW m⁻² K⁻¹ [9]. To develop a better understanding of thermal conductance values, it may be thought of in terms of an equivalent thermal thickness. Here one can equate the thermal resistance of an interface to the thermal resistance of a thin layer of a solid material, such as oxide. The equivalent thermal thickness is defined as $d_{\text{eq}} = k / G$, where k is the thermal conductivity of a solid and G is interface thermal conductance. For example, an interface with $G=100$ MW m⁻² K⁻¹ and a solid, such as oxide, with $k = 1$ W m⁻¹ K⁻¹, would give $d_{\text{eq}}=10$ nm. This implies that an interface with $G=100$ MW m⁻² K⁻¹ would offer the same amount of thermal resistance as a 10 nm thick layer of oxide. Since for typical solid-solid interfaces have interface thermal conductances in the range $8 < G < 300$ MW m⁻² K⁻¹, d_{eq} varies from approximately 3 to 125 nm of oxide.

Table 1: Summary of typical properties of electron and phonons

	Electrons	Phonons
Particle	Fermion	Boson
Wavelength, λ (nm)	0.1-1	1-5
Mean free path, l (nm)	10	10-100
Relaxation time, τ (fs)	10-100	(10-100)x10 ³
Propagation Speed, v (m/s)	$\approx 10^6$	(3-10)x10 ³

Two popular theories that can roughly predict the phonon mediated interface thermal conductance are the Acoustic Mismatch Model (AMM) and the Diffuse Mismatch Model (DMM). These theories are described in detail in chapter 2. The AMM apparently works well for low temperatures, while the DMM is a better approximation for higher temperatures when the mean free path and wavelength of the phonons become comparable to the physical and chemical roughness of the interface. Both of these models typically overpredict the actual interface thermal conductance.

1.3. Motivation

There is a growing interest towards miniaturization of devices and structures to exploit the unique and improved properties of materials at micro/nanoscales. With the recent advancements in the fields of microfabrication and nanoscale characterization, it is now possible to grow and analyze materials with atomic layer precision [10]. A better understanding of transport phenomena such as mass, charge, and heat is essential in designing and/or improving the performance of such nanoscale devices. Although charge

and mass transport at nanoscales have been studied extensively owing to the emergence of fields such as microelectronics and chemical and biological sensors, by comparison nanoscale heat transport has received little attention. The second law of thermodynamics requires that irreversible charge and mass transport must always be accompanied by heat transport with the environment. This heat transport may be useful or detrimental to the performance of the nanoscale device. Therefore, a detailed study of heat transport at the nanoscale is critical in improving the performance of low-dimensional devices.

Interfaces often dominate heat transport at the nanoscale, and they can greatly influence the operation and performance of nanodevices. For example, vertical cavity surface emitting lasers require that the heat generated within the superlattice structure be removed efficiently and rapidly. Therefore, interfaces with high thermal conductance are highly desirable. On the other hand, thermoelectric devices require that the active element has low thermal conductivity to improve the efficiency. In this case, multilayered nanostructures with low interface thermal conductance are highly preferred.

To have a better appreciation of the efforts to understand heat transport, we may look at the range of electrical and thermal conductivities of the most commonly found fully dense solids. At room temperature, the electrical conductivity spans a range of $\sim 10^{-16} - 10^8 \text{ S m}^{-1}$ for glasses and metals, while the thermal conductivity ranges from $\sim 1 - 10^3 \text{ W m}^{-1} \text{ K}^{-1}$ for the same materials. The approximately 24 orders of magnitude of variation in the electrical conductivity makes it easy to control the flow of electrons. However, excellent and poor thermal conductors are separated by only 3 orders of magnitude in thermal conductivity, thus it is extremely difficult to control the flow of heat. This fact is apparent from the daily life experience that even the best conductors of

heat present a significant amount of thermal resistance to heat flow and even the best insulators of heat conduct a significant amount of heat. On the other hand, electricity can be controlled with excellent precision. Electric current can be passed through a good charge conductor, such as copper wire, for miles without any significant losses as virtually no electricity leaks through the plastic insulator surrounding the copper wire. This easy control of charge transport is one of the reasons behind the success of the microelectronic industry.

If we can understand and control these mechanisms at the fundamental level, we will be able to tailor-make devices and materials depending on the requirement. For instance, a better understanding of heat transport between solid-solid and solid-liquid interfaces will greatly impact the thermoelectric [11-15] and thermionic [16-18] industries. In addition, it may also revolutionize the power electronics industry by providing better thermal management solutions [19-21]. Other areas of interest involve heat transfer fluids [22-24], thermal barrier coatings for gas turbine engines [25], photothermally and thermally activated drug delivery and medical therapies [26-29], and laser cavity cooling [6].

1.4. Objective

The objective of my doctoral dissertation is to study heat transport at the nanoscale. Specifically, this dissertation considers measurements (i) across dissimilar materials, and (ii) for low-dimensional structures. Low-dimensional structures are defined as structures that have at least one dimension confined in the range of nanometers such as superlattices, quantum dots, etc.

My work aims to develop a more complete understanding of heat transport at the nanometer lengthscales. There is a pressing need to understand various mechanisms that govern heat transport at the nanoscale. At the nanoscale, the mean free path and wavelength of different heat carriers become comparable to the size of the devices or structures themselves. Interface effects also become dominant and play a major role in defining the thermal characteristic of devices or structures. For instance, it was believed that carbon nanotubes could be employed in heat transfer fluids because they have the highest known thermal conductivity of any material in the world. However, Huxtable et al. found that the thermal transport of carbon nanotubes, dissolved in heavy water, has been severely affected because of the weak coupling between the carbon nanotubes and the surrounding surfactant [30]. This greatly limits the usefulness of these nanotubes for heat transfer applications. This example illustrates the importance of understanding the origins of interface conductance.

1.4.1. Scope of work

In this dissertation, I examine heat transport at interfaces between solid metals and solid nonmetals. There is an ongoing debate in the research community regarding the mechanisms responsible for the heat flow across such interfaces.

The flow of heat from a metal to a nonmetal requires that the energy carried by the electrons in the metal be transferred to the lattice of the nonmetal, where thermal energy is carried in the form of lattice vibrations (phonons). This energy can (a) be transferred directly from the electrons in the metal to the lattice of the nonmetal, or (b) may first be transferred from the electrons in the metal to the lattice of the metal and then to the

nonmetal via phonon-phonon coupling at the interface. The relative importance of each of these two pathways has remained difficult to assess experimentally. In the first research task, experiments are conducted to examine the difference in G by changing the structure of the metal (i.e. from amorphous to crystalline metallic alloys in this case) but not the composition. This work represents one of the first experimental studies to isolate the effect of structure apart from composition of a metal alloy and to quantitatively show that the structure of an alloy plays a measurable role in the interface conductance between metals and nonmetals.

My second research task involves studying the effects of nanoparticle size on the overall heat transport in nanocomposites. The thermal conductivity of nanoparticles, and the interface thermal conductance between the nanoparticles and the surrounding matrix provides useful insight into heat transport at the nanoscale. This work is one of the first experimental studies where the lower limits of thermal conductivity and interface thermal conductance of nanoparticles in a composite have been measured.

This dissertation is organized in the following manner. The second chapter discusses the fundamentals of nanoscale heat transport, and it also contains a literature survey. The third chapter describes the experimental techniques used to measure the thermal properties. The fourth and the fifth chapters present the results. The sixth chapter contains the conclusions of this work along with some future directions.

2. Background

In this chapter, the scattering mechanisms that dominate heat transport at the nanoscale are described in detail. The origins of the interface thermal conductance and theoretical models to describe it are also discussed. Finally, a literature review of the interface thermal conductance is presented.

2.1. Crystal vibrations

A typical energy-displacement diagram for a chemical bond is shown in Fig. 1. For small displacements around the equilibrium atomic spacing, x , the bond energy, E , is parabolic in nature. We may define $E = \frac{1}{2}Dx^2$, where D is some constant. Therefore, the interatomic force, F , can be calculated as follows, $F = -\frac{\partial E}{\partial x} = -Dx$. This is representative of simple harmonic motion (SHM), which implies that the chemical bond may be assumed as a spring and a solid crystal may be thought of as a 3-dimensional array of a spring-mass system as shown in Fig. 2.

For the simplicity of analysis, we will consider a 1-dimensional mono-atomic spring-mass system. When heat is supplied to this spring-mass system, it excites the atoms in the vicinity of the heat source causing them to be displaced from their equilibrium position [31-33]. If we perform a free body analysis on the n^{th} atom of mass m that is displaced by a distance of x_n from its equilibrium position, we obtain the following equation:

$$m \frac{d^2 x}{dt^2} = D(x_{n+1} + x_{n-1} - 2x_n) \quad (2.1)$$

where we assume that spring force on an atom is exerted only by its nearest neighboring atoms.

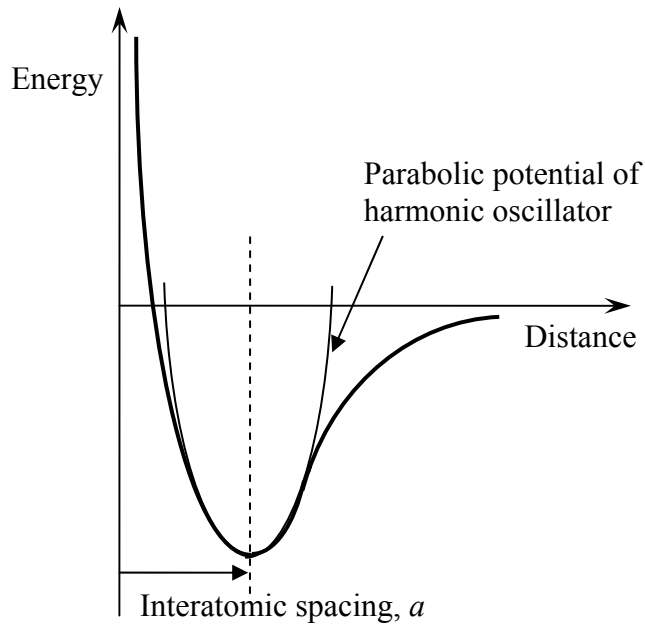


Figure 1: Energy-distance plot for an atom in a lattice. For small displacements around the equilibrium position, the atom may be considered as a simple harmonic oscillator.

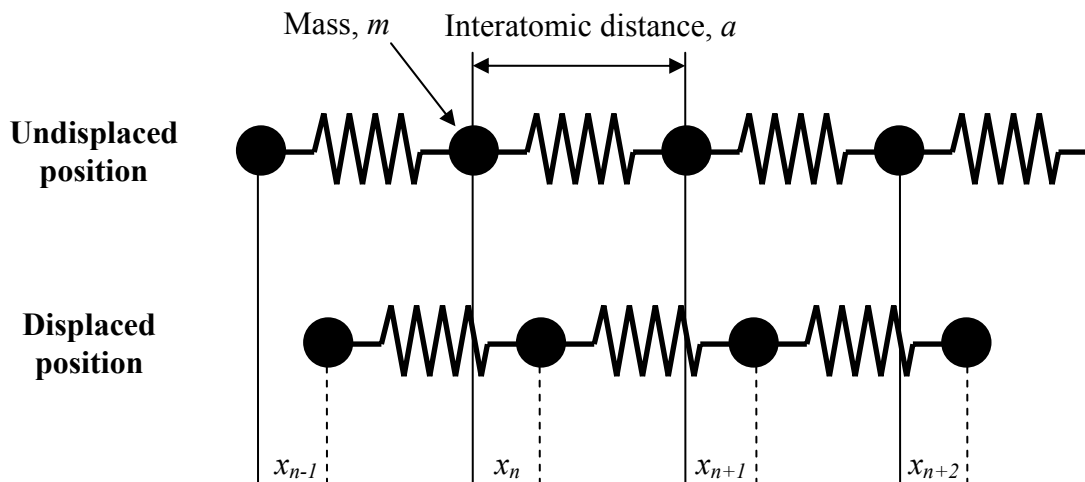


Figure 2: A spring-mass system. The atom and chemical bond are analogous to the mass and spring respectively.

The above relation represents an ordinary differential equation for the motion of atoms and its solution is linear in displacement. The solution for the above equation represents a wave: $x_n = x_0 \exp(-i\omega t) \exp(inKa)$, where ω is the angular frequency of the motion, a is the interatomic spacing, and $K = \text{wavevector} = 2\pi/\lambda$ with λ being the wavelength. The smallest λ that is possible within the crystal lattice is $2a$. This sets the limit on K : $-\pi/a < K \leq \pi/a$, which is defined as the first Brillouin zone. The center of the Brillouin zone is defined as the Γ point. Substituting this solution in equation (2.1) and solving, we have the following dispersion relation that relates ω and K :

$$\omega = \sqrt{\left(\frac{2D}{m}\right)(1 - \cos Ka)} = 2\sqrt{\frac{D}{m}} \left| \sin \frac{1}{2} Ka \right|. \quad (2.2)$$

The group velocity of a wavepacket is defined as the slope of ω - K curve, $v_g = \frac{d\omega}{dK} = \left(\frac{Da^2}{M}\right)^{\frac{1}{2}} \cos \frac{1}{2} Ka$. For long wavelength limits when $Ka \ll 1$, $\omega = \sqrt{\frac{D}{m}}(Ka) \Rightarrow v_g = a\sqrt{\frac{D}{m}}$. Thus, the frequency varies linearly with the wavevector and the group velocity becomes independent of the frequency and is equal to the speed of sound in the crystal. In this mode, the crystal vibrates similar to an acoustic wave and this branch is called acoustic phonon mode and is shown in Fig. 3. At the boundary of the Brillouin zone, $K = \pi/a$, $v_g = 0$ i.e. a standing wave is created and no information or energy is transported.

For diatomic crystals such as NaCl where there are two atoms in each unit cell, we have coupled equations of motion for displacements of the two atoms. When we solve these equations, in addition to getting the acoustic branch, we also get one solution where

atoms start vibrating against each other with their center of mass being fixed. This type of motion may be excited when light interacts with an electric dipole created by oppositely charged atoms in diatomic crystals such as NaCl. Therefore, this branch is called an optical branch and is shown in Fig. 3. The group velocity for the optical branch is zero or negligible for most of the Brillouin zone, hence this mode does not contribute significantly towards the overall heat transport.

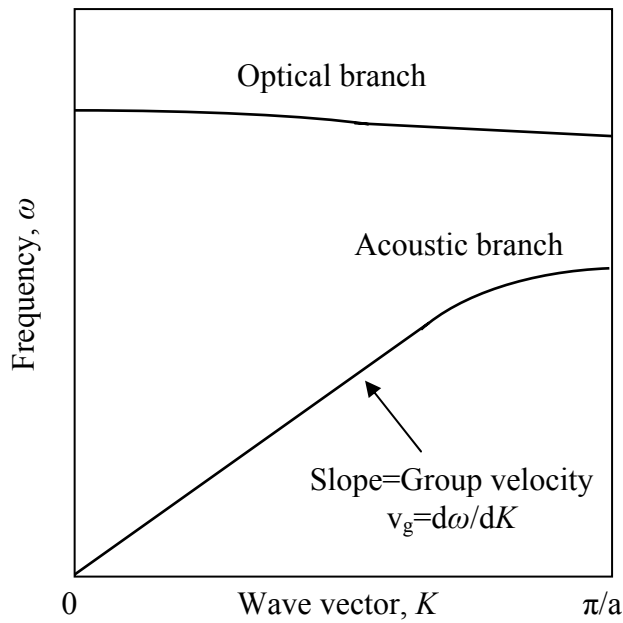


Figure 3: Phonon dispersion relation. The slope of the acoustic branch is defined as the group velocity of phonons.

2.2. Phonons

The energy and the amplitude of crystal vibrations are quantized. The quantum of vibrational energy is called a phonon. At the macroscale, the energy of a harmonic oscillator is defined as $E = \frac{1}{2} Dx^2$, and x and E are continuous. For a quantum mechanical oscillator, on the contrary, the energy and amplitude states are discretized.

The energy of a vibrational mode oscillating at an angular frequency ω is defined as,

$$E = (n + \frac{1}{2})\hbar\omega \quad (2.3)$$

where n is the number of phonons in that particular mode and \hbar is Planck's constant divided by 2π . Here, the term $\frac{1}{2}\hbar\omega$ is defined as the zero point energy of the mode. This implies that the crystal wave can occupy only certain allowable energy levels as shown in Fig. 4.

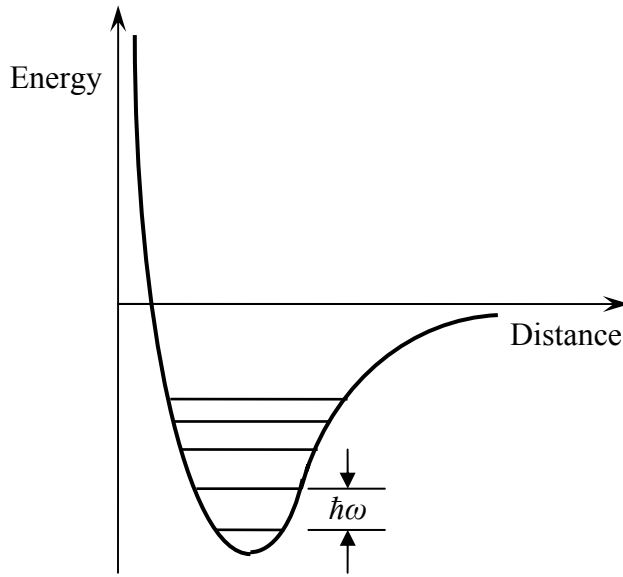


Figure 4: Quantum-mechanical oscillator. The phonon energy levels are discretized.

Phonons are analogous to photons in electromagnetic theory in many ways. The close analogy is attributed to the fact that both phonons and photons are a class of particles called bosons. The equilibrium number of phonons, $\langle n \rangle$, at a given temperature, T , is governed by Bose-Einstein distribution:

$$\langle n \rangle = \frac{1}{\exp\left(\frac{\hbar\omega}{k_B T}\right) - 1} \quad (2.4)$$

where k_B is Boltzmann's constant.

Therefore, the total energy of the lattice, E_l , can be defined as:

$$E_l = \sum_{K,p} \left(\langle n \rangle_{K,p} + \frac{1}{2} \right) \hbar\omega_{K,p}, \quad (2.5)$$

where K and p represent all wavevectors and polarizations respectively.

Phonons can also be treated as particles because the energy of a crystal wave containing a given number of phonons may be thought of as kinetic energy of the same number of particles in motion. This wave-particle duality holds true even during scattering processes because the waves scatter in a similar fashion as particles deflect when they collide.

Phonons are also assigned a momentum due to their particle nature. A particle in motion has a kinetic energy, E , of $E = \frac{1}{2}mv^2$, where m and v are the mass and velocity of the particle, respectively. The momentum, p , is defined as $p = mv \Rightarrow v = \frac{dE}{dp}$. The energy of a quantum harmonic oscillator is $E = \hbar\omega \Rightarrow v = \hbar \frac{d\omega}{dp} \Rightarrow dp = \hbar \frac{d\omega}{v} = \hbar dK \Rightarrow p = \hbar K$. The phonon momentum does not have a physical meaning but a phonon interacts with other phonons, photons or electrons as if it has a momentum $\hbar K$.

2.3. Phonon scattering

In solids, the phonons are scattered by colliding with defects, impurities, dislocations, other phonons, photons, and electrons. Knowledge of phonon scattering is important

when investigating heat transport in a solid. In an ideal world where there is no phonon scattering, there would be no resistance to heat transfer and a material will have infinite thermal conductivity.

Phonon scattering can be grouped in two classes: (i) elastic scattering of phonons by crystal imperfections where the energy and frequency of phonons are conserved, and (ii) inelastic scattering between interacting phonons where the frequency changes.

2.3.1. Scattering by crystal imperfections

Phonons may scatter as they encounter crystal imperfections such as defects, impurities, grain boundaries, or dislocations. The crystal imperfection acts as a site with a different mass and/or spring stiffness in the crystal lattice, thereby disrupting the incident phonon wave. This scenario may be imagined as throwing a stone in a water pond and observing ripples. As the ripple comes across small islands within the pond, it loses its strength. Here, throwing a stone in the pond is like providing thermal excitation to the solid, the ripples created are analogous to phonon waves, and the islands are imperfection sites.

Another way to describe this scattering phenomenon is using acoustic impedance, Z , of the lattice waves which is analogous to the index of refraction for the electromagnetic waves. The acoustic impedance is defined as: $Z = \rho v$, where ρ is the density of the material, and v is the speed of sound in the material. The speed of sound is defined as $v = \sqrt{C/\rho}$, where C is the stiffness of the chemical bonds. The imperfection may have different values of C and ρ when compared to the rest of the lattice resulting in an acoustic impedance mismatch at the imperfection site. This mismatch will cause the phonon to

scatter in similar manner as a photon does when it encounters a medium with differing index of refraction.

2.3.2. Inelastic scattering

Inelastic scattering involves three or more phonons where the frequency is altered. This process is also known as intrinsic scattering because this scattering may occur even in pure crystals.

Inelastic scattering occurs due to the anharmonic nature of the phonon waves. To explain this process, we consider a phonon wave propagating through the crystal lattice. As the wave transmits through the plane of atoms, the atoms are displaced from their equilibrium position. If the deformation of the spring is small, the spring stiffness is independent of the deformation. As the deformation becomes larger, the vibrations become more anharmonic in nature, and the spring stiffness changes with deformation. If another phonon wave is incident on this wave, it detects a change in the stiffness, and therefore a mismatch in the acoustic impedance. This causes the phonon wave to scatter.

Inelastic phonon-phonon scattering may involve three or more phonons. For the ease of explanation, we will consider only three phonon processes in next two sections. There are two types of such inelastic scattering: Normal (N) scattering and Umklapp (U) scattering.

2.3.2.1. Normal scattering

Normal or N scattering occurs when two phonons combine to produce a third phonon or a single phonon splits into two phonons without any change in total momentum during the

process. The process is shown in Fig. 5(a), (b). Energy and momentum are conserved in the process:

$$\omega_1 + \omega_2 = \omega_3, \quad \vec{K}_1 + \vec{K}_2 = \vec{K}_3 \quad \text{for the case in Fig. 5(a)} \quad (2.6a)$$

$$\omega_1 = \omega_2 + \omega_3, \quad \vec{K}_1 = \vec{K}_2 + \vec{K}_3 \quad \text{for the case in Fig. 5(b)} \quad (2.6b)$$

As energy and momentum are conserved in the N process, this type of scattering does not directly offer any resistance to heat flow. Since frequency is modified during the N process, N processes help distribute phonon energies over a wide range of frequencies. As other scattering processes are frequency dependent, N scattering indirectly affects heat transport.

2.3.2.2. Umklapp scattering

In Umklapp processes, the total momentum is not conserved. This situation arises when the vector addition of two combining phonons exceeds the boundary of the first Brillouin zone ($K=\pi/a$). Since wavelengths smaller than $2a$ are not possible in a crystal, phonons with wavevector larger than the Brillouin zone are not possible. The resultant phonon vector is brought back inside Brillouin zone by the addition of a reciprocal lattice vector, G , as shown in Fig. 5(c). The reciprocal lattice vector is defined as the vector joining the Γ points of the adjacent Brillouin zones. The third phonon vector direction is reversed in this process, resulting in smaller frequency and wavevector magnitudes. The energy and momentum equations are as follows:

$$\omega_1 = \omega_2 + \omega_3, \quad \vec{K}_1 + \vec{G} = \vec{K}_2 + \vec{K}_3. \quad (2.7)$$

As momentum is not conserved during the U process, this scattering mechanism directly poses resistance to heat flow. This process is responsible for the phonon mediated thermal conductivity of semiconductors and insulators at room temperature.

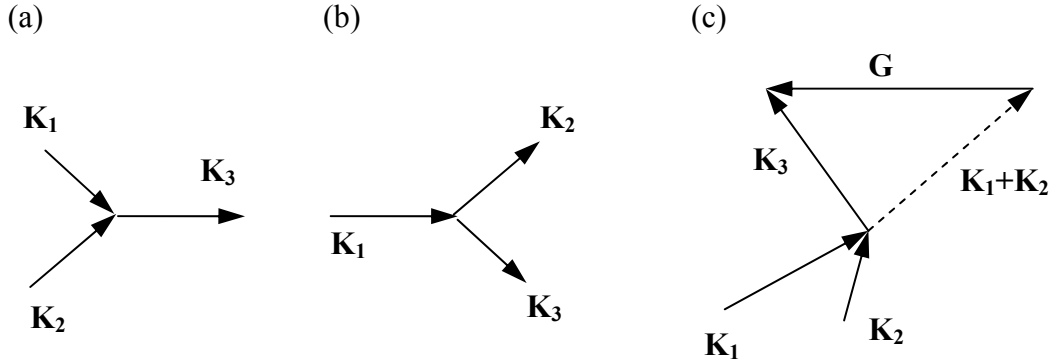


Figure 5: Phonon-phonon scattering. (a) two phonons combine to create a single phonon and the momentum is conserved, (b) one phonon splits into two phonons and the momentum is conserved, (c) two phonons combine to create a third one and the momentum during scattering is modified.

2.4. Temperature dependence of phonon scattering

Different scattering processes may dominate heat transport in a material depending on the temperature. This is due to the fact that the dominant wavelength of the phonon, λ_{dom} , and the temperature are related by an analogous Wien's displacement for phonons:

$$\lambda_{dom} = \frac{h\nu}{3k_B T},$$

where h is Planck's constant. At low temperatures, the dominant phonon

wavelength is so large that the phonons are not scattered by the defects. Moreover, as the dominant wavelength is large, corresponding wavevectors are small. Since large wavevectors are required for Umklapp scattering, this mechanism becomes unimportant, and phonon-phonon scattering is frozen out. Therefore, boundary scattering is the dominating mechanism at low temperatures as shown in Fig. 6. The phonon component of thermal conductivity, k_{ph} , is defined as $k_{ph} = \frac{1}{3} c_{ph} v_{ph} l_{ph}$, where c_{ph} is the phonon heat

capacity, v_{ph} is the speed of sound in the material, and l_{ph} is the mean free path of the phonons. At low temperatures, v_{ph} and l_{ph} are constant, and $c_{ph} \propto T^3$. Therefore, k_{ph} also varies as T^3 .

As the temperature increases, defect scattering becomes more dominant. This is due to the fact that the dominant phonon wavelength decreases as the temperature increases, and gradually becomes comparable to the size of the defects. This causes phonons to be scattered at the defect sites. For further increases in the temperature, wavevectors become so large that Umklapp scattering starts to play an important role.

A typical plot of phonon thermal conductivity of a material vs. temperature is shown in Fig. 6. For temperatures much smaller than the Debye temperature, as other scattering mechanisms are frozen out, boundary scattering is the dominating mechanism for heat transport. Debye temperature, θ_D , is defined as $\theta_D = \frac{h\omega_D}{k_B}$, where ω_D is the Debye cutoff frequency. In the middle range, where k_{ph} plateaus, impurity scattering is more important. At higher temperatures, U-scattering becomes dominant and we observe a decline in the thermal conductivity. It is to be noted that impurity scattering may dominate over much of the temperature range for alloys and doped semiconductors as they have large number of defects and impurities.

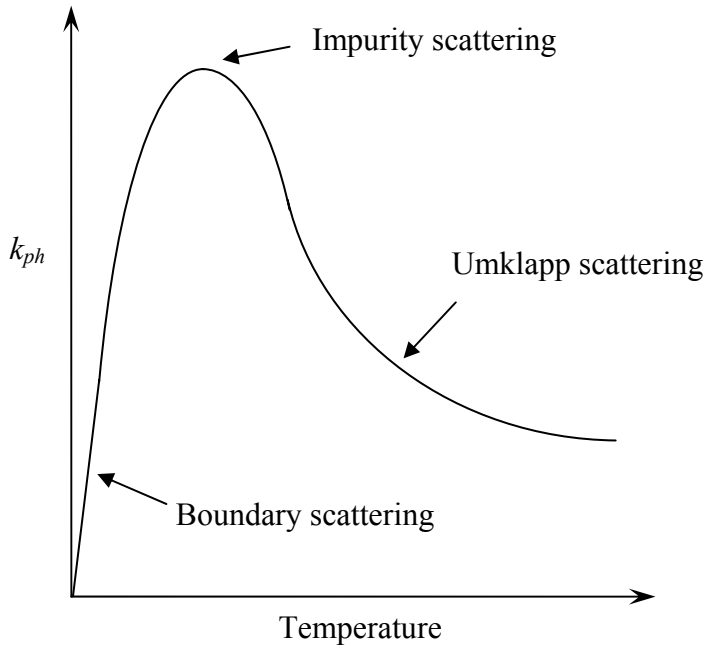


Figure 6: Temperature dependence of lattice thermal conductivity of solids. Boundary scattering dominates at lower temperatures, while impurity scattering becomes significant at intermediate temperatures. At high temperatures, inelastic scattering contributes considerably towards the overall thermal resistance.

2.5. Heat transport in low-dimensional structures

Heat transport in low-dimensional structures is significantly different compared to the bulk material due to the increased importance of size effects at such small lengthscales. As the size decreases, the surface area to volume ratio, which scales inversely with lengthscale, increases. Therefore, surface effects such as boundary and interface scattering become more dominant compared to volumetric effects such as defects and Umklapp scattering. A number of small-size mechanisms such as acoustic impedance mismatch, phonon spectra mismatch, phonon tunneling, and mini-bandgap formation start playing a major role towards the overall heat transport in the structure. The thermal

conductivity of a low-dimensional structure is usually smaller than the thermal conductivity of a corresponding bulk material.

2.6. Interface thermal conductance

All interfaces offer resistance to heat transport. As a heat flux is applied across the interface, a temperature drop is always observed across that interface. Interface thermal conductance, G , is defined as $G = q'' / \Delta T$, where ΔT is the observed temperature discontinuity across the interface for a supplied heat flux of q'' across the interface. The interface thermal conductance is also known as the thermal boundary conductance, and it is the inverse of the interface thermal resistance.

The presence of a thermal resistance at the interface will cause a momentum change of the heat carriers such as electrons and phonons as they *hit* the interface. The electron on the conductor side of the interface (i) either moves without any obstruction across the interface if the other side is also a conductor, (ii) or comes to a complete standstill at the interface if the other side of the interface is an insulator. As far as the phonon is concerned, it may or may not scatter depending upon various factors across interface.

The dominant phonon wavelength (λ_{dom}), defined as the wavelength in the entire phonon wavelength spectrum that carries the maximum amount of thermal energy, is evaluated using Wien's displacement law: $\lambda_{dom} = \frac{hv}{3k_B T}$, where v is the speed of phonon in the medium. Most solids have phonon propagation speed in the range of $v=1000-10000$ m/s. The interface would affect the approaching phonon in a similar way as a layer of impurity atoms would affect an incoming phonon, i.e. it would scatter the phonon. From

Table 2, we notice that λ_{dom} decreases with increasing temperatures. Therefore, the phonon will be scattered more at higher temperatures as λ_{dom} may become comparable to the size of the interface impurity atoms.

Table 2: The dominant wavelength of phonons in solids

$T(K)$	λ_{dom} (nm)	
	$v=1000$ m/s	$v=10000$ m/s
1	16	160
300	0.053	0.533

The existence of an interface thermal conductance was first proposed by Kurti, Rollin, and Simon in 1936 [34]. They suggested that this resistance would be too small and could be neglected. In 1941, Kapitza reported the first experimental measurement of thermal boundary resistance across an interface between liquid He and Cu [35]. Later in 1952, Khalatnikov developed an Acoustic Mismatch Model (AMM) to explain this thermal boundary conductance across He-solid interfaces [36]. In 1987, Swartz and Pohl developed a Diffuse Mismatch Model (DMM) for calculating the interface thermal conductance that captures the physics of phonon scattering at an interface at higher temperature [37]. In the following subsections, these models to describe interface thermal conductance are discussed.

2.6.1. Acoustic Mismatch Model (AMM)

In the AMM model, phonons are assumed as plane waves, and the media in which phonons propagate are considered as a continuous media (no lattice). This model defines a quantity, acoustic impedance, as the product of mass density and speed of sound in the material which is analogous to the index of refraction in optics. At an interface of dissimilar materials, due to the mismatch in acoustic impedances, phonons are scattered in the same way as an electromagnetic wave would scatter when it encounters a difference in refractive index. As the phonon wave encounters an interface, it may either (a) specularly reflect, (b) reflect and convert from a transverse to longitudinal mode, or vice versa, in manner that is called mode conversion, (c) refract, or (d) refract and mode convert as shown in Fig. 7. The final phonon wave may be a combination of these possibilities. The transmission coefficient may be calculated in a similar way as is done for the case of EM waves such as using Snell's law. The transmission coefficient, $T_{A \rightarrow B}$, for a phonon to transmit from material A to material B, when incident at an angle normal to the interface, is given as:

$$T_{A \rightarrow B} = \frac{4Z_A Z_B}{(Z_A + Z_B)^2} \quad (2.8)$$

where $Z = \rho v$ is defined as the acoustic impedance with ρ and v being the density and speed of sound of phonons on each side, respectively. One instance where AMM fails completely is at the interface between grain boundaries of identical materials, where AMM would predict a transmission coefficient of one. This example illustrates the drawback with the AMM in that it does not take into account the nature of the interface and it assumes reflection and transmission to be specular. The AMM is a good approximation when phonon wavelengths are much larger than the interatomic spacing.

The interface thermal conductance can be approximated as $Cv\alpha$, where C is the Debye volumetric specific heat, v is the Debye phonon velocity, and α is an averaged transmission probability.

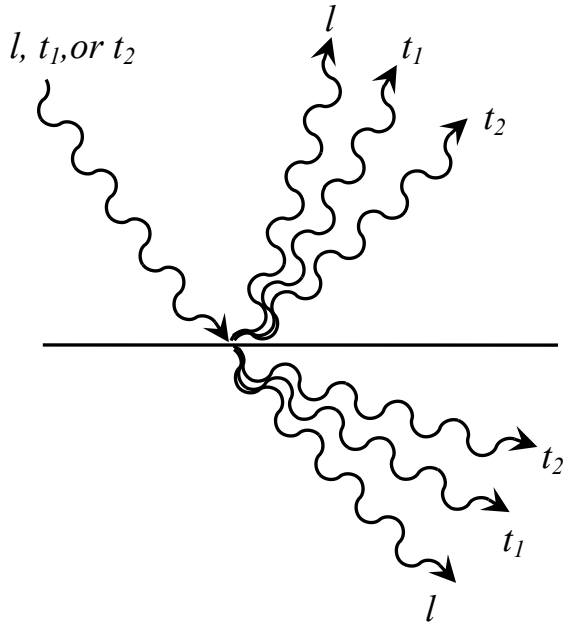


Figure 7: Scattering of a phonon at the interface. AMM assumes phonons to be analogous to photons, and the transmission and reflection probabilities are calculated using EM wave theory.

For a liquid He-Cu interface at temperatures below 100 mK, the AMM predictions for G were two orders of magnitude larger than the experimental values. At temperatures near 100 mK, the AMM interface thermal conductance seems to vary as T^3 and follows the same trend as the experiments but the magnitude is approximately a factor of three smaller than the experimental values [35, 37-40]. Above 1 K, the AMM underpredicts G by two orders of magnitude. The deviation is attributed to a contaminated surface and the presence of defects that may increase the phonon coupling across the interface. The high interface conductance is attributed to the attenuation of phonons in bulk solids near the interface, caused by electrons and dislocations [41, 42].

In 1959, Little extended the AMM to interfaces between solid materials [43]. Early work in the 1960s and 1970s on indium-sapphire interfaces found that the AMM overpredicts G at low temperatures (~ 1 K). Swartz measured G across various solid-solid interfaces [44] and observed that the AMM is in line with the experiments below 40 K, but above 40 K the model overpredicted G .

2.6.2. Diffuse Mismatch Model

At higher temperatures, the dominant phonon wavelength, which scales as the inverse of the temperature, is smaller, and therefore, in this regime, high frequency phonons dominate the heat flow. For high frequency phonons (>100 GHz), the physical and chemical roughness of an interface becomes comparable to the wavelength of the dominant heat carrying phonons, making phonon reflection and transmission less specular [45]. Therefore, the AMM does not describe heat transport that well at higher temperatures. To resolve this issue, Swartz and coworkers proposed a Diffuse Mismatch Model (DMM) [37]. The DMM assumes that when a phonon strikes an interface, it loses memory of where it came from. The probability of transmission across the interface depends on the ratio of the phonon density of states in the materials. The DMM assumes elastic scattering at the interface and thus the frequency of the phonon does not alter during scattering at the interface. The elastic scattering also implies that an incident phonon will never scatter into multiple lower frequency phonons or that multiple numbers of phonons will never scatter into higher frequency phonons.

For temperatures below 1 K, the DMM predictions of G for liquid He-Cu interfaces are two orders of magnitude higher than the AMM. The experimental observations for

nonmetallic solids seem to match reasonably well with DMM predictions at room temperature [5].

AMM works well for temperatures below 30 K [37]. Swartz and Pohl [37] compared G using AMM and DMM for various combinations of solid materials at low temperatures [37]. They found that there is only $\pm 30\%$ of difference between the two models for solid-solid cases. A qualitative plot of ratio of the DMM to AMM thermal interface conductance with a parameter that represents dissimilarity across the interface for low temperatures is shown in Fig. 8. This dissimilarity parameter may be defined as $[Z_{\text{large}}/Z_{\text{small}}-1]$, where Z_{large} and Z_{small} are the larger and smaller acoustic impedances of the two sides across the interface, respectively. Fig. 8 shows that diffuse scattering decreases G for similar solids, while it increases G for highly dissimilar solids. Another interesting point to note is that for highly dissimilar interfaces such as He/Cu, the diffuse model predicts even smaller G .

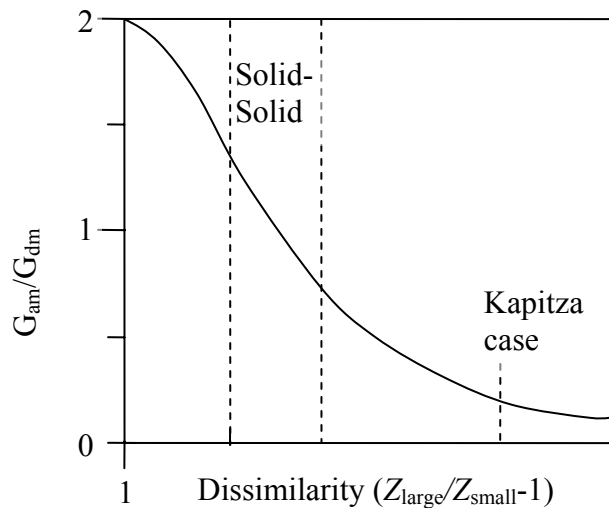


Figure 8: Plot of ratio of interface thermal conductances predicted by DMM and AMM, respectively, as a function of the amount of mismatch. The dissimilarity may be thought of as $[(\rho c_{\text{max}}/\rho c_{\text{min}}) - 1]$. The Kapitza case represents Cu-liquid He interfaces.

At higher temperatures, the experimentally observed interface thermal conductance tends to deviate from AMM predictions, and the DMM gives a better picture of G . One possible explanation for G is the discontinuity in the phonon density of states across the interface. At higher temperatures where a full spectrum of vibrational modes is thermally excited, the measured interface thermal conductance is in poor agreement with the theoretical models.

2.6.3. Phonon radiation limit

The phonon radiation limit predicts the maximum interface thermal conductance when phonons are assumed to be scattering elastically at the interface [46]. The phonons from the side having the lower phonon density of states are assumed to have transmission probability of one. On the other hand, only a limited number of phonons from the material with the higher phonon density are assumed to transmit such that the principle of detailed balance and second law of thermodynamics is satisfied. Since the radiation limit ignores inelastic scattering processes, which are often dominate in solid-solid interfaces, in most cases it underpredicts G .

2.7. Literature survey on interface thermal conductance

There is only a limited amount of data available in the literature for measurements of interface conductance between solid-solid interfaces. This is due to the difficulty in fabricating abrupt interfaces without damages, and lack of reliable experimental techniques to measure G . With the advancements in microfabrication and measurement techniques in the past 10-15 years, there has been growing interest to understand and

control G . This section summarizes some of these recent important experimental studies on the interface thermal conductance.

Stoner and Maris [47] used a picosecond optical technique to measure G between metal-dielectric interfaces between 50 and 300 K. In their study, the range of Debye temperatures for metals was between 102 to 426 K, while for dielectrics the Debye temperature varied between 287 to 2200 K. The values of G for these metal-dielectric interfaces at room temperature are given in Table 3. For the majority of these interfaces, it was observed that the materials with similar Debye temperatures had higher values of G . Lattice dynamics (LD) simulations were used to predict G . For materials with Debye temperatures differing by less than a factor of 5, the experimentally measured G matched well with the LD predictions. However, the experimental G was larger by as much as one order of magnitude compared to the LD model for materials with highly mismatched Debye temperatures. This suggests that inelastic processes and the anharmonicity in the metal may be playing a key role in transporting the heat across the interface.

The authors also examined another aspect of heat transfer across metal-nonmetal interfaces: how important is the electron-phonon coupling across the interface? They prepared two similar samples by depositing ~ 100 nm of Pb on diamond, except that one sample had ~ 3.5 nm thin intermediate layer of Bi between Pb and diamond. It is to be noted that Pb and Bi have very similar phonon spectra, so it was expected that the Bi layer would not significantly affect the phonon flux incident from the Pb side. On the other hand, Bi is a semimetal, and it has a much smaller electron density compared to Pb which is a metal. Therefore, it is expected that the electrons from the Pb side would be greatly impeded by the Bi layer and the cooling rate for the Pb-Bi-diamond sample would

be much smaller than the Pb-Bi sample. However, cooling curves for both samples were found to be very similar. The authors suggested that coupling of the electrons in the metal and phonons in the dielectric does not contribute significantly towards the heat transport across the interface.

Hubermann and Overhauser [48] interpreted the Pb/diamond interface data obtained by Stoner and Maris by introducing the concept of electronic conductance at the Pb/diamond interface. They suggested that Pb and diamond atoms oscillate in joint vibrational modes near the interface. The majority of the energy of these joint modes resides with atoms on the diamond side, and therefore these joint vibrational modes have temperatures equal to the temperature of the diamond side. The temperature difference between electrons at Pb temperatures and the joint vibrational modes at diamond temperatures causes energy transfer across the interface.

Table 3. Measured interface thermal conductance for metal-dielectric interfaces at room temperature [47]. The temperature in parenthesis represents the Debye temperature of the material.

G (MW m ⁻² K ⁻¹)	Pb (102 K)	Au (165 K)	Al (423 K)	Ti (426 K)
BaF2 (287 K)	62	40	100	
Sapphire (1024 K)	55	45	105	112
Diamond (2240 K)	31	40	46	100

Costescu et al. [49] measured G across interfaces between epitaxially grown TiN and single crystal oxides such as MgO and Al₂O₃ at temperatures between 79.4 K to 294 K. The data was found to be in good agreement with the LD and DMM predictions. The

room temperature G for the interfaces was found to be $\sim 700 \text{ MW m}^{-2} \text{ K}^{-1}$, which was a factor of seven larger than what Stoner and Maris [47] found for a similar interface between metal/ Al_2O_3 . The reason for this difference could be due to the higher frequencies of acoustic modes in TiN, e.g. the averaged longitudinal speed of sound in TiN is ~ 1.6 times larger than Al. However, the authors attributed the bulk of the difference to the perfect abruptness of the interface. It was claimed that the results were a true indicator of the intrinsic heat transport at the interface due to the absence of electron or phonon scattering by defects at the near interface regions of the substrate and film.

Stevens et al. [50] measured G for a series of metal-dielectric interfaces that are listed in Table 4. They determined that, in general, the materials with large difference in the Debye temperatures have smaller G compared to materials with similar Debye temperatures. It was concluded that the phonons of a particular frequency can couple only with the same frequency phonons in the other material. If there is large mismatch in Debye temperatures, then the transmission probability for phonons is smaller, resulting in smaller value of G . The DMM was used to calculate G , and was compared with measured values of G . For interfaces with a Debye temperature ratio greater than 0.4, the DMM overpredicts G ; while for dissimilar materials, the DMM underpredicts.

Gundrum et al. measured G for metal-metal interfaces [51]. They found G for Al/Cu interfaces to be $\sim 4 \text{ GW m}^{-2} \text{ K}^{-1}$ at room temperature, an order of magnitude higher than typical metal-dielectric interfaces. The magnitude and temperature dependence of G fits well with a DM model for electron transport at the interface. Since the phonon contribution and elastic scattering at metal-metal interfaces is small, a Wiedemann-Franz law [52] was developed for predicting G for such interfaces.

Lyeo et al. conducted an interesting study to qualitatively determine the relative importance of two mechanisms that govern heat transport across metal-nonmetal interfaces. The majority of heat in metals is carried by electrons while phonons transport most of the heat in nonmetals due to the absence of free electrons. Therefore, at a metal-nonmetal interface, heat may be transported only via two possible pathways as shown in Fig. 9. In the first pathway, electrons within the metal transfer their energy to the phonons in the metal through a direct anharmonic electron-phonon coupling across the interface. In the second pathway, electrons transfer their energy to phonons within the metal, followed by phonon-phonon coupling across the interface. Lyeo et al. [9] measured G for interfaces between materials with highly dissimilar Debye temperatures such as Bi and Pb (having low Debye temperatures), with dielectrics and semiconductors (having high Debye temperatures). They found that G for interfaces between Bi, a semimetal, and interfaces with Pb, a metal, fall within a small range, $8 < G < 30 \text{ MW m}^{-2} \text{ K}^{-1}$. It is worthwhile to mention that Pb and Bi have very similar phonon spectra, yet the electronic heat capacity of Pb is approximately 600 times larger than that of Bi. If the thermal transport across the metal-nonmetal interface were to be dominated by direct electron-phonon coupling across the interface, G for Pb/dielectric interfaces would greatly exceed that of Bi/dielectric interfaces. Therefore, a relatively narrow range of G suggests that the coupling between electrons in the metal and the phonons in dielectric does not contribute significantly towards the G .

The authors also found that for highly dissimilar materials above 40 K, the measured G increases linearly with increasing temperature. The molecular dynamics (MD) simulation of G assuming inelastic scattering of phonons for Pb/diamond interfaces

shows that G increases linearly with increasing temperature. This suggests that the anharmonic processes such as three phonon processes are important for heat transport across the interface. Although the measured G for interfaces between Bi and H-terminated diamond is found to be extremely low ($G=8.5 \text{ MW m}^{-2} \text{ K}^{-1}$), it is much larger than the phonon radiation limit. These results are significantly different than results obtained by Stoner and coworkers, where G for Pb/Diamond interfaces was found to be independent of temperature ($T>100 \text{ K}$). The authors claim that the hydrogen-terminated diamond substrate provides for a chemically cleaner interface.

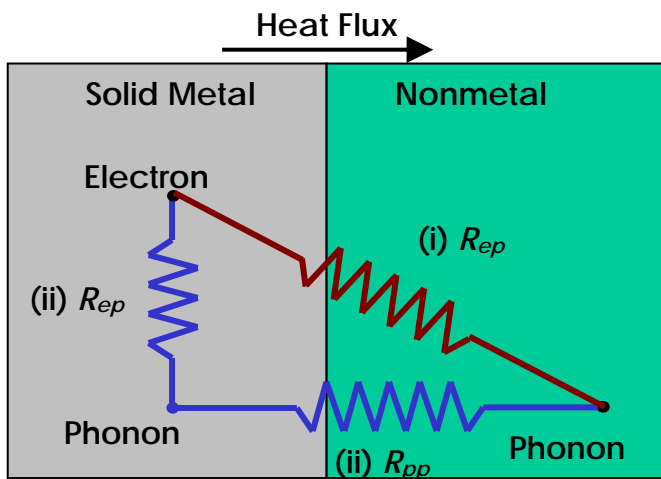


Figure 9: Two pathways for heat carrier coupling at a metal/nonmetal interface: (i) the heat may either be transferred directly from the metallic electrons to the nonmetallic phonons, (ii) or heat is first transferred from electron to phonons within the metal and subsequently thorough phonon-phonon coupling across the interface.

In summary, it is found that for phonon-mediated heat transport across an interface, G typically falls in a narrow range of 8 to $300 \text{ MW m}^{-2} \text{ K}^{-1}$ with a notable exception of $G=700 \text{ MW m}^{-2} \text{ K}^{-1}$ for TiN/MgO interfaces (see Table 4 and Fig. 10).

Majumdar and Reddy [53] estimated the thermal conductance associated with electron-phonon coupling in a metal/metal-nonmetal interface as $G_{ep} = \sqrt{Ck_p}$, where C is the volumetric electron-phonon coupling constant and k_p is the lattice component of the thermal conductivity in the metal. It was also theoretically shown that $G_{ep} \propto 1/\sqrt{T}$ for temperatures near the Debye temperature of the metal and that G_{ep} near the metal-nonmetal interface is of the same order as the experimentally observed G . The DMM and experimental data match well when G_{ep} is included in the DMM for predicting G for TiN/MgO interfaces measured by Costescu and coworkers [49]. This strongly suggests that the electron-phonon coupling in the metal near the metal-nonmetal interface contributes significantly towards the overall heat transport.

Kosevich [54] theoretically showed that for soft/hard interfaces, the contribution of inelastic scattering (subharmonic and multiharmonic) towards G is much larger compared to the elastic scattering. Sergeev, Il'in, and coworkers [55, 56] proposed the existence of inelastic electron scattering at the interface of a conducting film and an insulating substrate at low temperatures ($T <$ Debye temperature). This inelastic electron scattering opens up new channels for heat transport from film electrons to the substrate phonons. The contribution of this inelastic electron scattering towards interface thermal conductance is approximated to be 20-60 MW m⁻² K⁻¹ which is of the order of observed G for dissimilar materials. This inelastic electron scattering also determines the temperature dependence of thermal resistivity.

Table 4: Compilation of measured interface thermal conductance of important solid-solid interfaces

Interface	G (MW m⁻² K⁻¹)	Reference
Au/SiO ₂ /Si	50	[57]
Au(78nm)/LaAlO ₃	100	[58]
YBaCuO(300nm)/LaAlO ₃	12.5	[58]
TiN/MgO	700	[49]
TiN/Al ₂ O ₃	~650	[49]
Al/Sapphire	200	[50]
Cr/Sapphire	190	[50]
Au/Si	71	[50]
Pt/Si	140	[50]
Al/Si	120	[50]
Cr(30nm)/Si	200	[50]
Al/GaN	190	[50]
Cr/GaN	230	[50]
Al/AlN	230	[50]
Cr/GaN	200	[50]
Al/Cu	4000	[51]
Cu/Al ₂ O ₃	110	[51]

Interface	G (MW m⁻² K⁻¹)	Reference
Bi/H-diamond	~8	[9]
Bi/H-Si	~11	[9]
Pb/Diamond	~19	[9]
Pb/H-diamond	~15	[9]
Pb/H-Si	~19	[9]

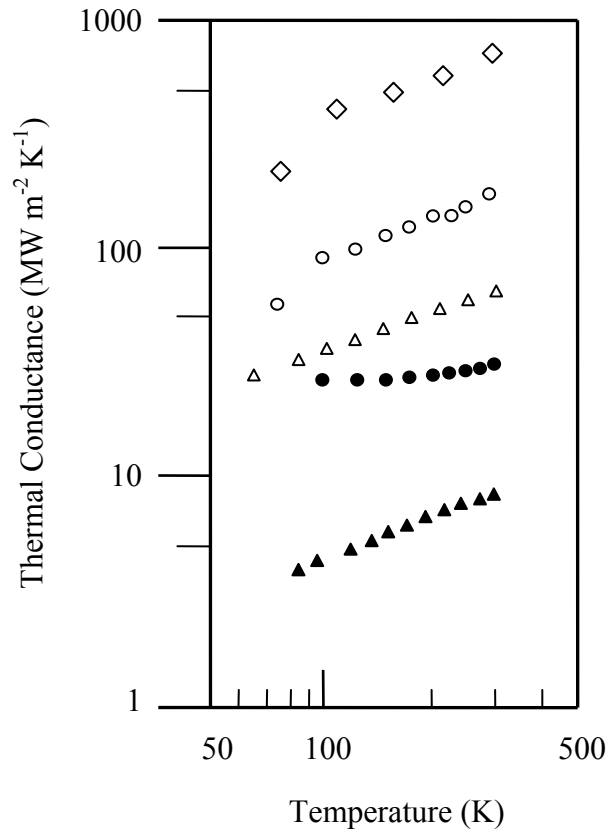


Figure 10: Summary of experimental data taken for the interface thermal conductance for various solid-solid interfaces with temperature. The interfaces are represented as follows: TiN/MgO by open diamond (\diamond), Al/Al₂O₃ by open circles (\circ), GST/ZnS:SiO₂ by open triangles (Δ), Pb/diamond by filled circle (\bullet), and Bi/H-diamond by filled triangle (\blacktriangle). The data is taken from reference [9].

3. Experiments

Thermal conductivity characterization of bulk materials has been done extensively, and accurate measurement techniques are available to determine thermal conductivity [59-61]. Remarkably, there are not many techniques available to measure thermal properties of thin films and low-dimensional structures [5, 6]. For cross-plane (perpendicular to the film plane) thermal conductivity measurements, many traditional techniques require that one determines the temperature drop across the film thickness, which may range from micrometers to nanometers. It is difficult to create a measurable temperature drop across the film without creating a large temperature rise in the substrate. In these situations, measuring the temperature drop across such a thin film becomes a difficult task in itself. Several different strategies have been adopted to resolve such issues. In this chapter, I discuss two techniques that we are using for measuring thermal properties of thin films and nanostructured composites.

3.1. 3- ω Method

The 3- ω method was developed by Cahill [62] to measure thermal conductivity of bulk materials, and later it was extended for films as thin as tens of nanometers [57]. This method involves depositing a thin and narrow layer of metal on top of the thin film of interest as shown in Fig.1. This metal layer acts both as a heater and a thermometer.

A sinusoidal AC current with frequency ω , $I(t) = I_0 \cos \omega t$ is passed along the metal strip producing Joule heating of $P = I^2 R = I_0^2 R \cos^2 \omega t = \frac{I_0^2 R}{2} (1 + \cos 2\omega t)$, where R is the resistance of the metal line.

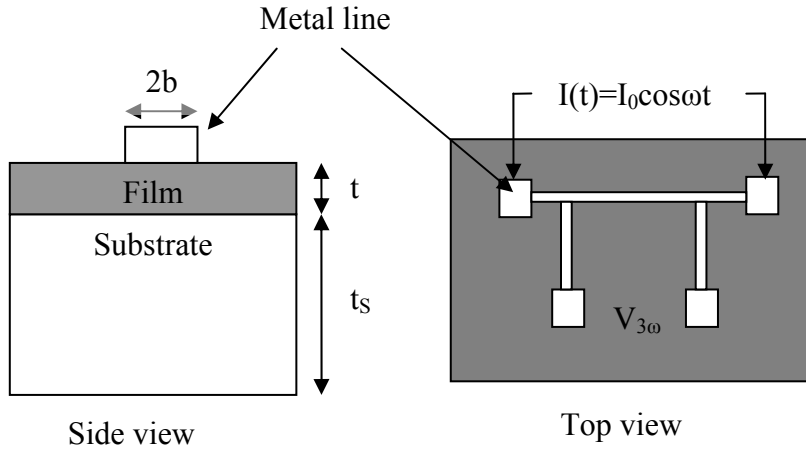


Figure 11: 3ω method for measuring thermal conductivity of thin films and bulk solids. A thin layer of a metal is deposited on the surface of samples, and the metal acts as both a heater and a thermometer.

Since heating is modulated at a frequency of 2ω , the temperature also oscillates at the 2^{nd} harmonic of ω (2ω), i.e. $T = T_{DC} + T_{2\omega} \cos 2\omega t$. Now, as the resistance of a pure metal is linearly proportional to temperature, the resistance also has a 2ω component, i.e.

$$R(t) = R_0 \left(1 + \frac{dR}{dT} T \right), \text{ where } \frac{dR}{dT} \text{ is the temperature coefficient of resistance.}$$

The voltage difference across the strip can be calculated as

$$\begin{aligned}
V(t) &= I(t)R(t) = (I_0 \cos \omega t)R_0 \left(1 + \frac{dR}{dT} (T_{DC} + T_{2\omega} \cos 2\omega t)\right) \\
&= I_0 R_0 \cos \omega t + I_0 R_0 \cos \omega t \frac{dR}{dT} T_{DC} + I_0 R_0 \cos \omega t \frac{dR}{dT} T_{2\omega} \cos 2\omega t \\
&= I_0 R_0 \cos \omega t + I_0 R_0 \cos \omega t \frac{dR}{dT} T_{DC} + \frac{I_0 R_0 T_{2\omega}}{2} \frac{dR}{dT} (\cos 3\omega t + \cos \omega t) \\
&= I_0 R_0 \cos \omega t + I_0 R_0 \cos \omega t \frac{dR}{dT} T_{DC} + \frac{I_0 R_0 T_{2\omega}}{2} \frac{dR}{dT} (\cos 3\omega t + \cos \omega t) \\
&= I_0 R_0 \cos \omega t + I_0 R_0 \cos \omega t \left(\frac{dR}{dT} T_{DC} + \frac{I_0 R_0 T_{2\omega}}{2} \frac{dR}{dT} \right) + \frac{I_0 R_0 T_{2\omega}}{2} \frac{dR}{dT} \cos 3\omega t
\end{aligned} \tag{3.1}$$

The double underscored term is third harmonic, i.e. the 3ω component of the voltage.

$$\Rightarrow V_{3\omega} = \frac{I_0 R_0 T_{2\omega}}{2} \frac{dR}{dT} \tag{3.2}$$

Therefore, the temperature amplitude of the heater is given as:

$$\Rightarrow T_{2\omega} = \frac{2V_{3\omega}}{I_0 R_0} \frac{dT}{dR} = \frac{2V_{3\omega}}{V_{1\omega}} \frac{dT}{dR} \tag{3.3}$$

Present day lock-in amplifiers can easily measure the 1ω as well as the 3ω voltage component. The thermal model used to calculate thermal conductivities of films and substrates has 3 underlying assumptions.

(1) It assumes the metal heater to be a line source of heating. This implies that the half width of line heater b must be much smaller than the penetration depth of the thermal wave in the substrate $d = \sqrt{\alpha/\omega}$, where α =thermal diffusivity of the substrate, i.e. $b \ll d$

(2) It is also assumed that width of heater $2b$ is much larger than the film thickness t , i.e. $2b \gg t$. This ensures that heat conduction in the film is 1-D.

(3) The substrate is assumed to be semi-infinite. This implies that the thermal penetration depth d is much smaller than the substrate thickness t_s , i.e. $d \ll t_s$.

The temperature amplitude of the heater can be written as

$$T_{S+F} = T_S + T_F = T_S + \frac{pd_F}{2blk_F} \quad (3.4)$$

where d_F =film thickness, p =power amplitude dissipated per unit length of heater, l =length of heater, k_F =film thermal conductivity, T_S =Temperature rise at the film-substrate interface.

From assumptions (1) and (2), the temperature amplitude of the heater at a radius r from the heat source can be written as:

$$T_S = \frac{p}{\pi k_S} \left(\frac{1}{2} \ln \frac{\alpha}{r^2} + \ln 2 - 0.5772 - \frac{1}{2} \ln(2\omega) - \frac{i\pi}{4} \right) \quad (3.5)$$

where α is thermal diffusivity and k_s is the thermal conductivity of the substrate. The thermal conductivity of the substrate is thus calculated from the slope of the real (i.e. in-phase) part of the voltage signal (V_{in}) as a function of $\ln(\omega)$ and equation (3.3) as follows:

$$k_S = \frac{V^3 \ln \frac{\omega_2}{\omega_1}}{4\pi R^2 (V_{3\omega,1} - V_{3\omega,2})} \frac{dR}{dT} \quad (3.6)$$

The film thermal conductivity is then calculated from equation (3.4).

The 3ω method has been built and studied in our nanoscale heat transport lab. A LabVIEW Virtual Instrument (VI) has been built to completely automate data acquisition. A lockin amplifier and temperature controller are remotely controlled by PC using an RS232 communication interface. A Pyrex sample has been tested to validate the setup. The thermal conductivity was measured from 80-300 K and the data are shown in Fig. 12. The data agree well with values found in the literature.

One of the major drawbacks of the 3ω method is its inability to distinguish between thermal conductivity and interface thermal conductance. It cannot directly measure interface thermal conductance. The method also requires that the top surface of a sample is electrically insulating. Thus conducting samples must first be coated with a thin insulating film.

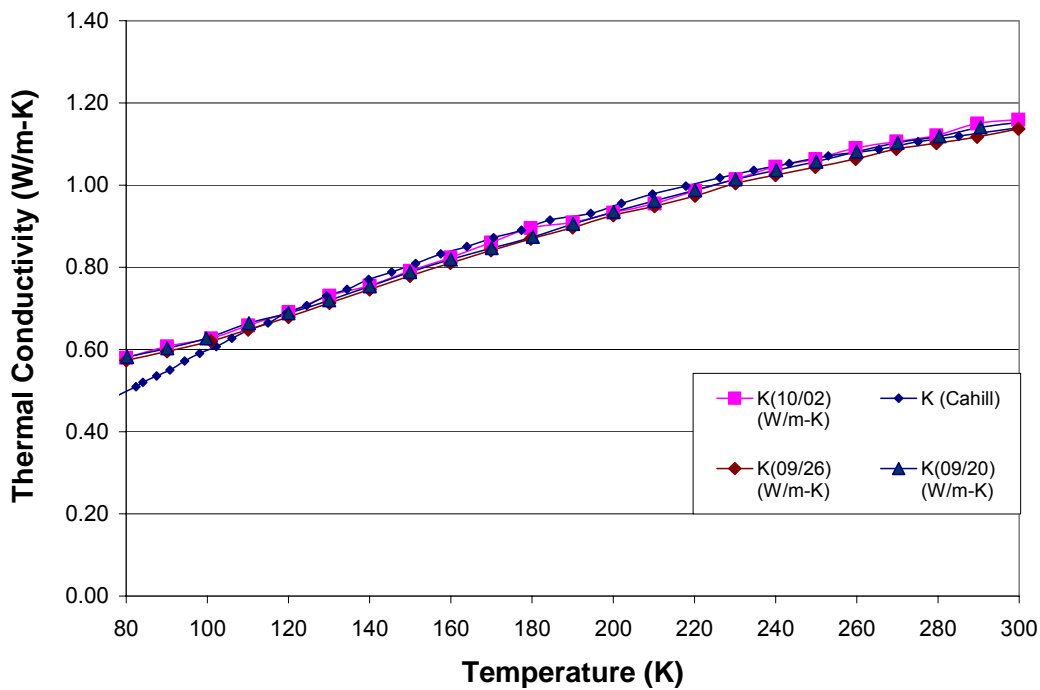


Figure 12: Temperature measurement of thermal conductivity for a Pyrex sample. The data are taken on three different dates and compared with the data collected by Cahill [63] on a similar type of Pyrex.

3.2. Time Domain Thermo-Reflectance (TDTR) technique

With advancements in the field of high speed lasers in the last two decades, various non-contact optical techniques have been developed for thermophysical property characterization [64-68]. Time domain thermoreflectance has proven to be one of the

most powerful techniques [49, 69-71]. This technique was originally developed by Paddock and Eesley [64] and by Capinski and coworkers [68]. Later, Cahill [72] modified the technique to improve the accuracy of the measurements, and recently Huxtable and coworkers have successfully used the technique for quantitative thermal conductivity imaging with a resolution of $\sim 3 \mu\text{m}$ [70]. The two major advantages with TDTR are that (i) it is a non-contact technique and requires little to no sample preparation, and (ii) the technique quantitatively measures thermal conductivity and interface thermal conductance simultaneously.

In short, TDTR is a pump-probe method where laser radiation from a pump beam is used to heat the sample and the decay of the surface temperature is measured using a time delayed probe laser beam. An ultra-fast laser beam with pulse duration of ~ 100 fs, repetition rate of ~ 80 MHz and wavelength $\lambda=800$ nm is split into pump and probe beam using a 50:50 beamsplitter. The pump is modulated at ~ 10 MHz to improve the signal-to-noise ratio (SNR) through the use of lock-in detection. A schematic diagram of the TDTR system is shown in Fig. 13. The technique takes advantage of the fact that the reflectivity of metals has a small but measurable dependence on temperature. For a small temperature rise, the reflectivity is linearly proportional to the temperature rise. A thin layer (~ 80 - 100 nm thick) of metal, such as aluminum, that has high thermorefectance in the near infrared range is deposited on the surface of the sample. The pump heat pulse is focused on the sample, and the laser energy is absorbed within the optical thickness of Al (≈ 25 - 30

nm). The time constant for the temperature to stabilize within Al is $\tau = \frac{d_{Al}^2}{\pi^2 \alpha_{Al}}$, where α_{Al} is thermal diffusivity of Al and d_{Al} is the film thickness. At room temperature, $\tau \approx 25$ ps, i.e. redistribution of energy inside Al is complete within 25 ps. The temperature of Al film

decays after this redistribution time as heat diffuses through the interface between the Al and through the underlying substrate. A time delayed probe beam is then focused on the same spot of the sample, and changes in the reflectivity of the Al film are measured using a photodiode detector and lock-in amplifier. This change in reflectivity is related to the surface temperature, and thus we can measure the temporal decay of surface temperature.

This experimental data is then compared with a heat transport model for layered geometries. Unknown parameters such as thermal conductivity and interface thermal conductance are then adjusted until the results from theoretical model fits with the experimental data.

The heat transfer model considers the frequency domain solution for a semi-infinite solid that is heated at surface by a periodic point source of unit power at angular frequency ω [2]

$$g(r) = \frac{\exp(-qr)}{2\pi kr} \quad (3.7)$$

$$q^2 = \frac{i\omega}{\alpha} \quad (3.8)$$

where k = thermal conductivity, α = thermal diffusivity, r = radial coordinate. Due to the cylindrical symmetry of the TDTR experiment [72], we can use the Hankel transform of $g(r)$ as

$$G(K) = 2\pi \int_0^{\infty} g(r) J_0(2\pi Kr) r dr = \frac{1}{k(4\pi^2 K^2 + q^2)^{1/2}} \quad (3.9)$$

The Gaussian distribution for the energy in the pump beam is

$$p(r) = \frac{2A}{\pi w_0^2} \exp\left(-\frac{2r^2}{w_0^2}\right) \quad (3.10)$$

where A = the amplitude of heat absorbed by sample at frequency ω , $w_0=1/e^2$ radius of the pump beam.

The Hankel transform of $p(r)$ is

$$P(K) = A \exp\left(-\frac{\pi K^2 w_0^2}{2}\right) \quad (3.11)$$

The surface temperature $\theta(r)$ is the inverse transform of the product of $G(K)$ and $P(K)$

$$\theta(r) = 2\pi \int P(K)G(K)J_0(2\pi Kr)KdK \quad (3.12)$$

The probe beam measures a weighted average of the temperature distribution $\theta(r)$

$$\begin{aligned} \Delta T &= \frac{4}{w_1^2} \int_0^\infty \theta(r) \exp\left(-\frac{2r^2}{w_1^2}\right) r dr \\ &= 2\pi A \int_0^\infty G(K) \exp\left(-\frac{\pi^2 k^2 (w_0^2 + w_1^2)}{2}\right) K dK \end{aligned} \quad (3.13)$$

where $w_1=1/e^2$ radius of the probe beam.

Equation (11) can be applied to a layered geometry using the Feldman algorithm [73].

$G(k)$ in equation (11) is defined as

$$G(k) = \frac{1}{\gamma_1} \left(\frac{B_1^+ + B_1^-}{B_1^+ - B_1^-} \right) \quad (3.14)$$

$$\text{where } \begin{pmatrix} B^+ \\ B^- \end{pmatrix}_n = \frac{1}{2\gamma_n} \begin{pmatrix} \exp(-u_n L_n) & 0 \\ 0 & \exp(u_n L_n) \end{pmatrix} \begin{pmatrix} \gamma_n + \gamma_{n+1} & \gamma_n - \gamma_{n+1} \\ \gamma_n - \gamma_{n+1} & \gamma_n + \gamma_{n+1} \end{pmatrix} \begin{pmatrix} B^+ \\ B^- \end{pmatrix}_{n+1},$$

$$u_n = (4\pi^2 K^2 + q_n^2)^{1/2}, \quad q_n^2 = \frac{i\omega}{\alpha_n}, \quad \gamma_n = k_n u_n.$$

The algorithm assumes $n=1$ for the layer that absorbs all of the heat, i.e. the aluminum layer on the surface of the sample. The layer below the aluminum is assigned $n=2$ and so on. The iteration starts with the layer farthest from the aluminum, i.e. the substrate in our case. For all practical purposes, heat cannot reach the far side of the

bottom layer in these experiments, thus $B^+=0$ and $B^-=1$ for the substrate. The model also includes the thermal conductance for each interface.

The signal of interest is produced by the product of temperature changes and the intensity of the probe beam. The time delay between the pump and probe beam shifts the relative phase of the probe frequency spectrum, and the lock-in amplifier picks the frequency components of convolution at f and $-f$:

$$\text{Re}[\Delta R_M(t)] = \frac{dR}{dT} \sum_{m=-M}^M (\Delta T(m/\tau + f) + \Delta T(m/\tau - f)) \exp(i2\pi mt/\tau) \quad (3.18a)$$

$$\text{Im}[\Delta R_M(t)] = -i \frac{dR}{dT} \sum_{m=-M}^M (\Delta T(m/\tau + f) - \Delta T(m/\tau - f)) \exp(i2\pi mt/\tau) \quad (3.18b)$$

where R represents the reflectivity, f is the pump modulation frequency in Hz, τ is the repetition rate of the laser and $i = \sqrt{-1}$. The real and imaginary parts correspond to the in-phase (V_{in}) and out-of-phase (V_{out}) voltage signals measured by the lock-in amplifier.

3.2.1. Experimental setup

For our TDTR setup, we use a Ti:Sapphire femtosecond laser that operates at a repetition rate of 80 MHz with a pulse duration of ~ 100 fs, and wavelength range of 750-850 nm. A schematic diagram of the setup is shown in Fig. 13. The laser pulses exiting the laser cavity are split into pump and probe beams using a 50:50 non-polarizing beamsplitter. Since the beam diameter is large (mm scale) when it arrives to the TDTR setup, a Keplerian type of telescopic lens system is used to reduce the pump and probe beam diameters.

The pump beam passes through an electro-optic modulator (EOM), where it is modulated (typically at 10 MHz) with s-polarization. This s-polarized pump beam is then

incident on a polarizing beam splitter at a right angle, where almost 99% of the beam is reflected towards an objective lens. This objective lens serves three primary purposes: i) it focuses the beam to a small diameter ($\sim 25 \mu\text{m}$), ii) it collimates the reflected pump and probe beams, which is essential in improving the signal to noise ratio, and iii) it is used to image the sample on a CCD camera. The CCD camera allows us to see the sample, and it greatly aids in focusing and aligning the pump and probe beams on the sample. The reflected pump beam is blocked out using a beam block which absorbs most of the reflected pump energy. This prevents the pump beam from reaching the photodetector and corrupting the reflected probe beam signal.

The arrival of the probe beam at the sample is delayed using a mechanical delay stage that can provide delays of ~ 2 ns. Subsequently, the probe beam passes through a 50:50 beamsplitter and the same objective lens as the pump beam. The probe beam is directed along the center line of the objective lens, and is focused on the same spot of the sample where the pump beam is focused. The pump and probe beams are separated by $\sim 4\text{-}5$ mm when they enter the back of the objective lens. The reflected probe beam is collected in a photodiode detector. An RF lock-in amplifier measures the photodiode signal at the pump modulation frequency. To increase the magnitude of the signal, an inductor is connected in series to the photodetector to create a resonant circuit that amplifies the signal. For instance, a quality factor of ~ 7 is obtained when using an inductor of $17.2 \mu\text{H}$ at a resonant frequency of 9.8 MHz. The two channels of the RF lock-in amplifier are used to measure the in-phase (V_{in}) and out-of-phase (V_{out}) signals. We use the ratio of the in-phase and out-of-phase voltages (V_{in}/V_{out}) for calculating the thermal properties as it reduces the non-idealities in the system such as defocusing of the

beams, and the variations in pump-probe overlap. These non-idealities tend to affect the in-phase and out-of-phase signals in the same manner, thus the ratio is relatively insensitive to these errors.

The data can easily be corrupted if scattered energy from the pump beam is allowed to reach the detector. For flat and smooth samples, a combination of a beam blocker and irises in the paths of the pump and probe beams, respectively, prevents most of the reflected pump beam from reaching the detector. For rough surfaces, some of the pump beam may be scattered into the detector resulting in poor signal to noise ratio (SNR). To improve the SNR, we employ different approaches such as using optical filters and a double modulation technique.

Using optical filters involves spectrally separating the pump and probe beams. Optical high pass and low pass sharp edge filters with cutoff wavelength close to the laser wavelength are placed in the paths of the pump and probe beams, respectively. This modifies the spectral configuration of pump and probe beams as shown in Fig. 15. Then another low pass filter with the same cutoff wavelength is placed right before the photodetector. It becomes apparent from Fig. 15 that this low pass filter will allow most of the reflected probe to go through, while removing most of the reflected pump from reaching the photodetector. Therefore, this approach significantly improves SNR.

The double modulation frequency technique involves modulating the probe beam frequency in low audio frequency (AF) ranges of ~ 200 Hz to 1 KHz using a mechanical chopper. This causes the probe signal to have the following frequency components: f , f_{chopper} , $(f + f_{\text{chopper}})$ and $(f - f_{\text{chopper}})$, where f is the laser frequency and f_{chopper} is the chopper frequency. The thermorelected signal is essentially the product of pump and probe

signals. Therefore, the thermoreflected signal contains following frequency terms: $(f + f_{\text{mod}})$, $(f - f_{\text{mod}})$, $(f_{\text{mod}} + f_{\text{chopper}})$, $(f_{\text{mod}} - f_{\text{chopper}})$, $(f + f_{\text{mod}} + f_{\text{chopper}})$, $(f - f_{\text{mod}} + f_{\text{chopper}})$, $(f + f_{\text{mod}} - f_{\text{chopper}})$, and $(f - f_{\text{mod}} - f_{\text{chopper}})$, where f_{mod} is pump modulation frequency. The photodetector signal also contains scattered pump signals at f_{mod} . As this signal from the detector is fed to the RF lock-in amplifier, it is multiplied by an external reference set at f_{mod} . If no filter is selected, the output from the RF lock-in will contain a d.c. component due to the scattered pump and thermoreflectance signal at frequency f_{chopper} . The V_{in} and V_{out} signals from the radio-frequency (RF) lock-in amplifier are then input to two separate audio-frequency (AF) lock-in amplifiers which are referenced at the chopper frequency, f_{chopper} . Since the scattered pump signal does not contain any frequency component at the chopper frequency, it is eliminated as a d.c. voltage signal. Therefore, the resultant voltage outputs from the respective AF lock-ins correspond to V_{in} and V_{out} thermoreflectance signals without any pump noise. This greatly improves the SNR of the signal for rough samples.

The electronics and equipment involved in controlling the EOM and the acquisition of the signal is schematically explained in Fig. 14. The output signal from the EOM is tested by setting a low frequency of 0.5 or 1 Hz on the function generator. The bias voltage is then adjusted until we observe the output beam modulating at the set frequency.

A LabVIEW VI built specifically for the TDTR experiments handles all of the data acquisition and communication between the PC, delay stage, and the lock-in amplifier, as shown in Fig. 16. Typical signal versus time plots are shown in Fig 13.

A Fortran code is written to mimic the thermal conduction model for 1-D multilayer structures using theory as described in the previous section. The unknown thermal

parameters such as thermal conductivity and interface thermal conductance are adjusted in the code so as to minimize the difference between results from the model and the experimental data. The program also includes the effects caused by variations in the probe beam diameter with increasing optical length. The code is attached as Appendix A.

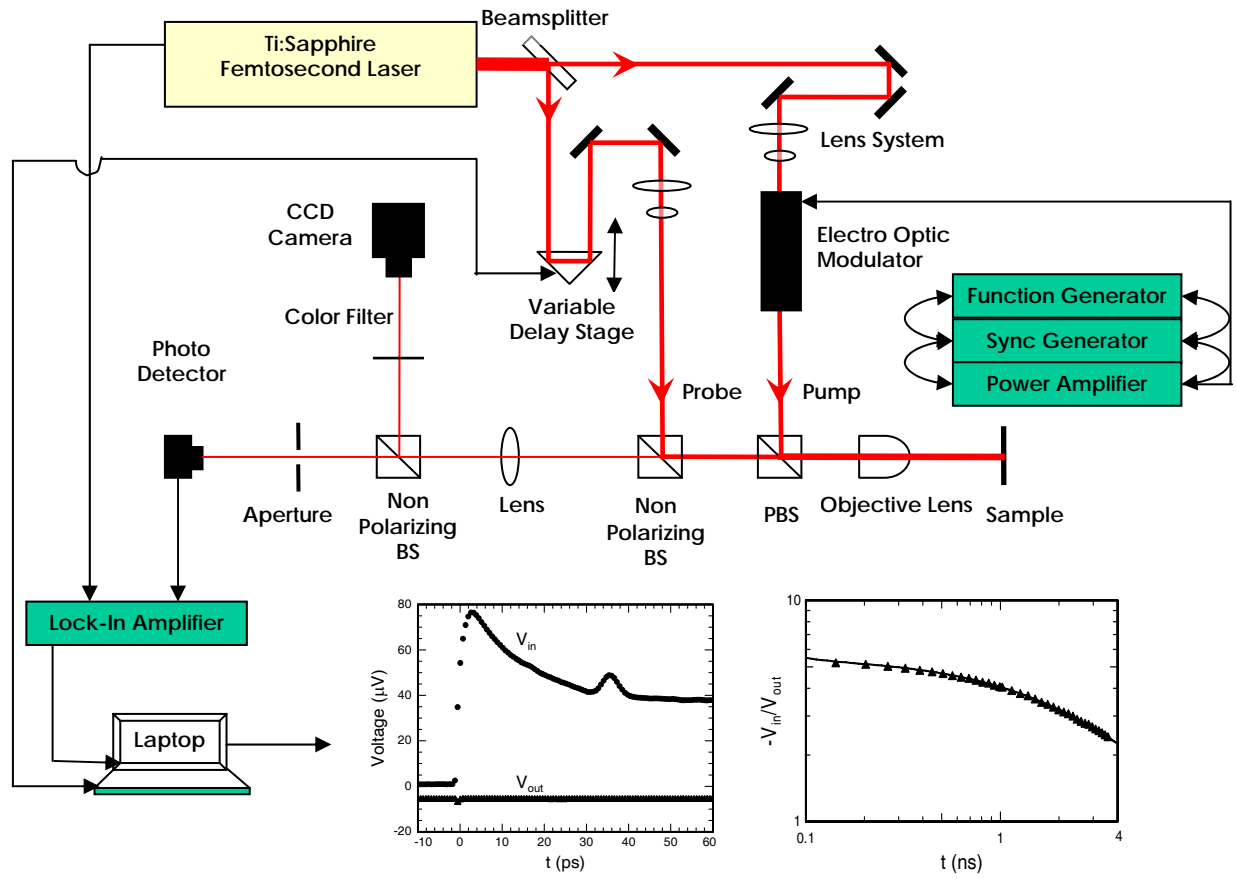


Figure 13: Time-domain thermoreflectance (TDTR) setup. Femtosecond laser pulses are split into pump and probe beams using a beamsplitter. The pump beam is modulated at ~ 10 MHz using an electro-optic modulator. The probe beam passes through a delay stage that provides time delay with respect to the pump. The pump and probe are focused on the same spot using an objective lens and a CCD camera. The reflected probe is collected by a photodetector, and then fed to a RF lock-in amplifier to improve SNR. The thermoreflectance signal, in the form of in-phase (V_{in}) and out-of-phase (V_{out}) voltages from lock-in, is recorded using a computer. The ratio ($-V_{in}/V_{out}$) is used in the analysis as it reduces the errors caused by non-idealities in the system such as defocusing of probe beam.

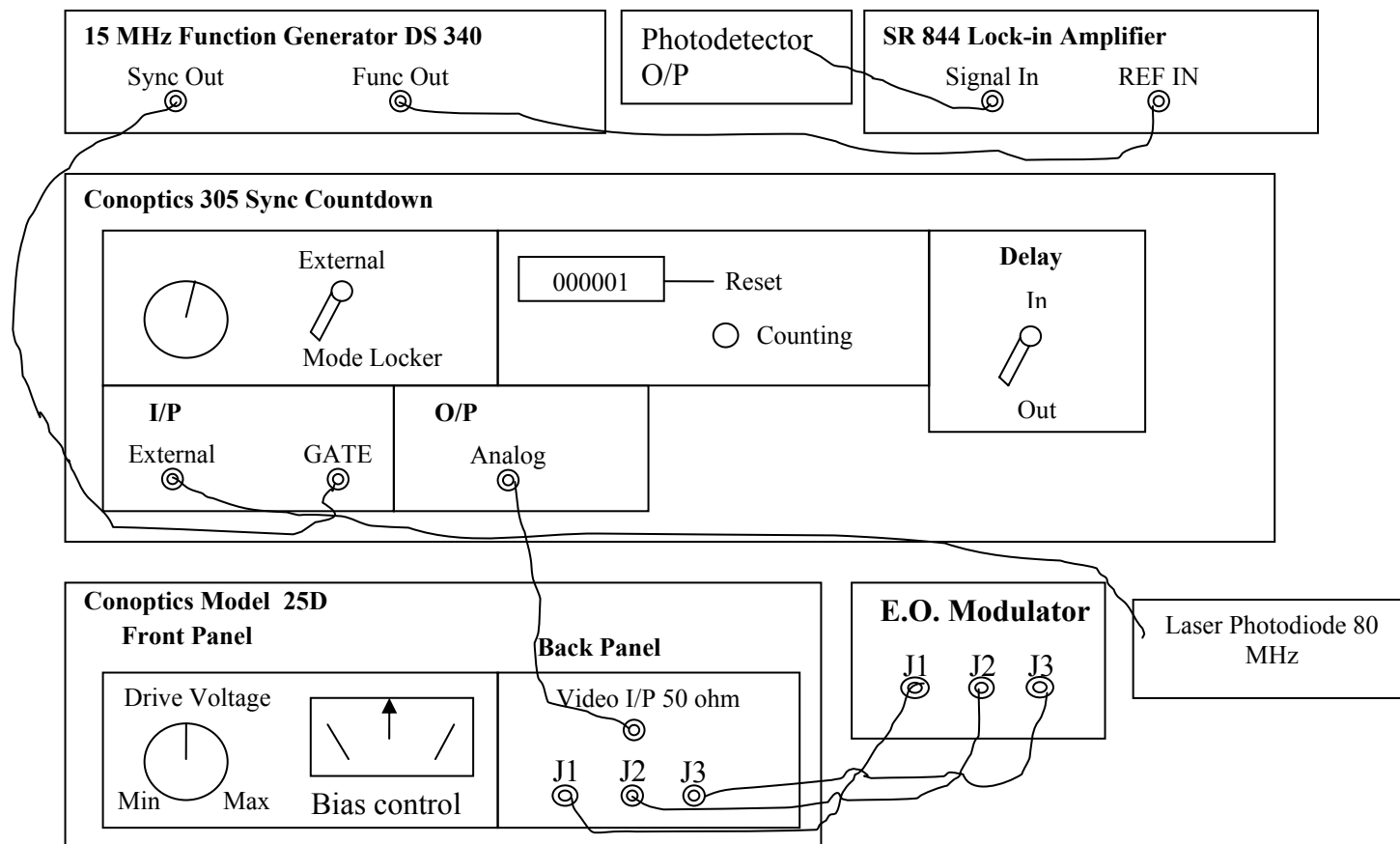


Figure 14: The electronics associated with the modulation of the pump beam and the measurement of thermorefectance signal using a RF lock-in amplifier. A Conoptics 25D line amplifier drives an E.O. Modulator (350-160). A Conoptics 305 sync countdown provides the timing and delay adjustments that are required for laser pulse-picking. The modulation frequency is controlled using a Stanford Research Systems DS340 function generator. The RF lock-in is referenced using the "Func Out" output from the function generator.

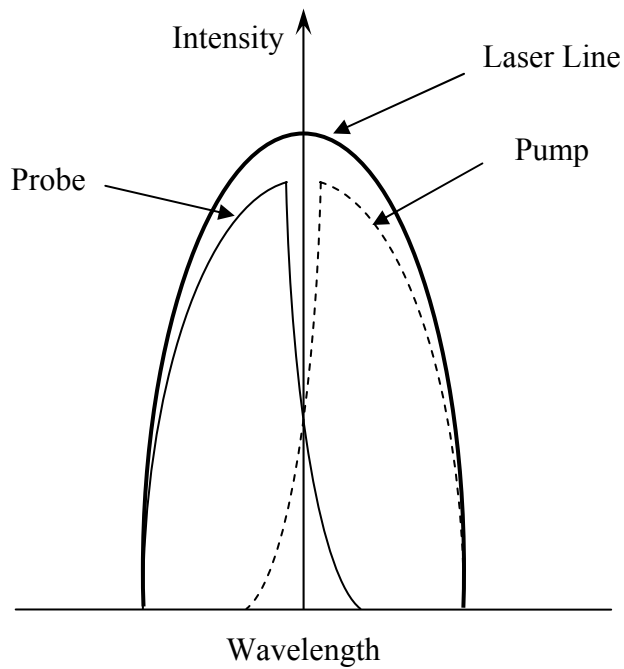


Figure 15: Use of optical filters for efficient rejection of reflected pump. High pass and low pass optical filters with cutoff wavelengths near the laser wavelength are placed in the pump and probe paths, respectively. The thick solid line represents the wavelength spectrum of laser, while the thin solid and dashed lines are probe and pump wavelength spectrums after the optical filters, respectively. Notice that only a small fraction of the reflected pump will pass through the low pass filter that is placed immediately before the photodetector.

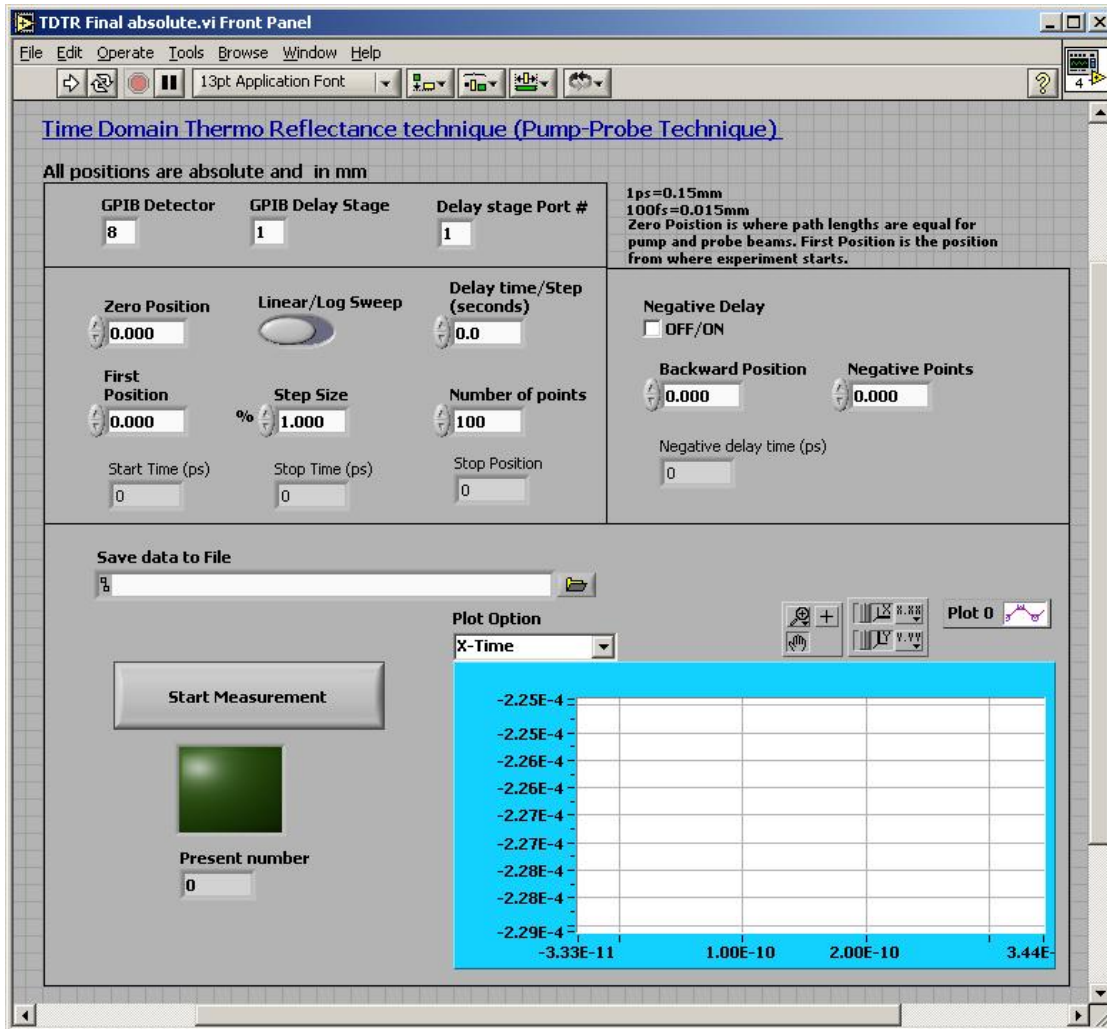


Figure 16: TDTR LabVIEW program. The LabVIEW VI is used to control the movement of the delay stage and to acquire the voltage signals from the lock-in amplifier. The data is saved as an electronic file.

3.2.2 Verification of the TDTR setup

The TDTR setup is tested with three different samples: plasma enhanced chemical vapor deposition (PECVD) grown SiO₂, fused quartz, and sapphire samples. The data (i. e., the ratio of $-V_{in}/V_{out}$) for each of the three samples is compared with a heat transfer model for multilayer structures as shown in Fig 17. The thermal conductivity values for ~600 nm

thick PECVD grown SiO₂, fused quartz, and sapphire samples are determined to be 1.15, 1.28, and 36 W m⁻¹ K⁻¹, respectively, at room temperature.

The thermal conductivity values found using TDTR are similar to the values found in the literature for PECVD grown SiO₂, fused quartz, and sapphire. Kleiner et al. [74] measured $k=1.1$ W m⁻¹ K⁻¹ for a 1.19 μm thick PECVD oxide layer, while Huxtable [75] et al. measured $k\sim 1$ W m⁻¹ K⁻¹ for a 120 nm thick layer of PECVD oxide using the 3ω technique. The literature values found for the thermal conductivity of fused quartz are as follows: 1.23 [76], 1.38 [77], 1.3 [78] W m⁻¹ K⁻¹. The thermal conductivity of sapphire falls in a wide range: 30 [79], 33 [80], 36 [77], 43 [81] W m⁻¹ K⁻¹.

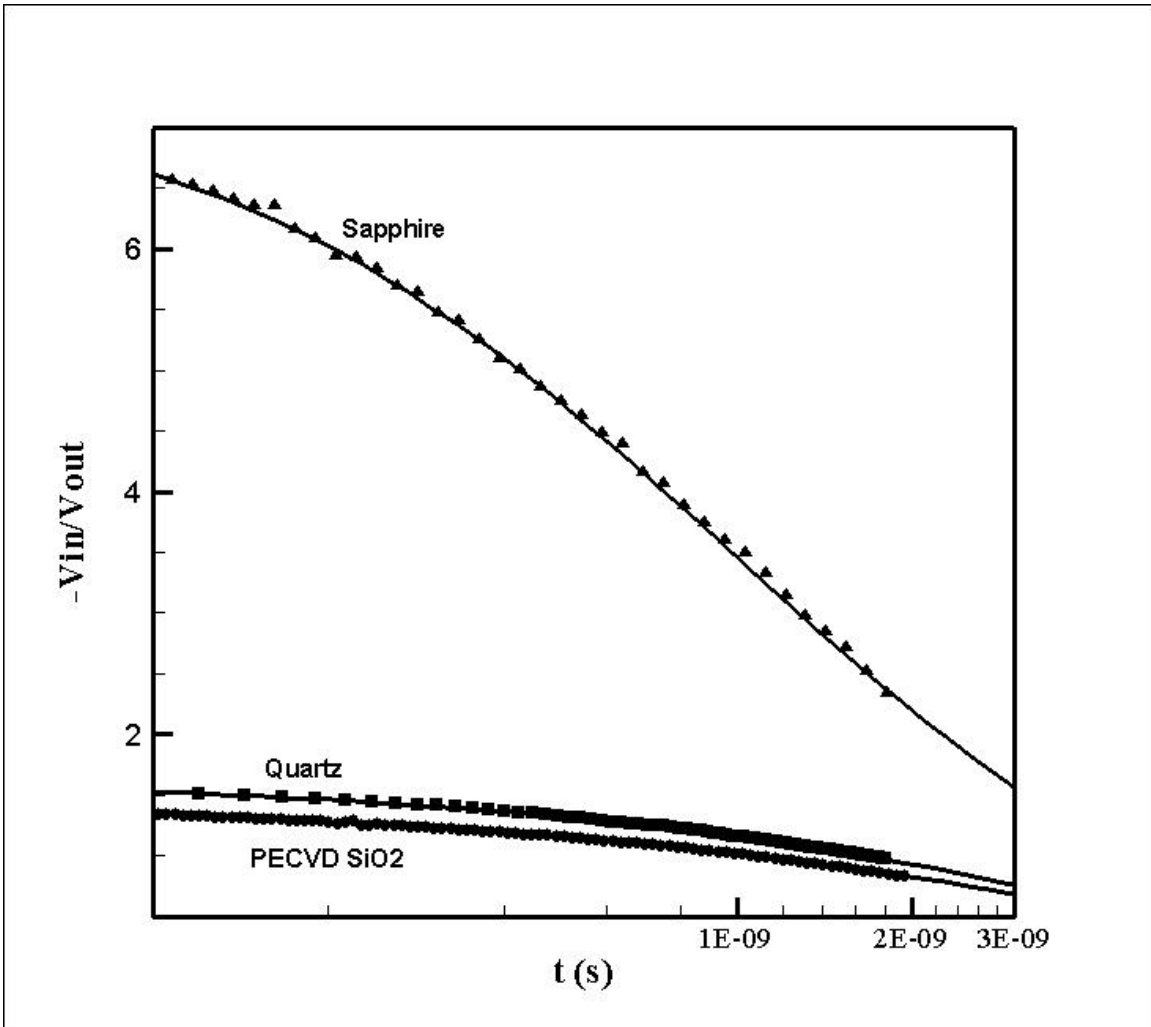


Figure 17: TDTR signal for PECVD oxide, fused quartz, and sapphire samples. The solid lines for each sample represent the best fit thermal model.

4. Thermal conductivity and interface thermal conductance of amorphous and crystalline $Zr_{47}Cu_{31}Al_{13}Ni_9$ alloys with a Y_2O_3 coating[†]

4.1. Abstract

In this chapter, the thermal conductivity, k , and interface thermal conductance, G , for amorphous and crystalline $Zr_{47}Cu_{31}Al_{13}Ni_9$ alloys in contact with poly-crystalline Y_2O_3 are examined. The time-domain thermoreflectance method discussed in the previous chapter is used to measure these thermal properties. TDTR finds $k=4.5 \text{ W m}^{-1} \text{ K}^{-1}$ for the amorphous metallic alloy of $Zr_{47}Cu_{31}Al_{13}Ni_9$, and $k=5.0 \text{ W m}^{-1} \text{ K}^{-1}$ for the crystalline $Zr_{47}Cu_{31}Al_{13}Ni_9$. TDTR also gives $G=23 \text{ MW m}^{-2} \text{ K}^{-1}$ for the metallic glass/ Y_2O_3 interface and $G=26 \text{ MW m}^{-2} \text{ K}^{-1}$ for the interface between the crystalline $Zr_{47}Cu_{31}Al_{13}Ni_9$ and Y_2O_3 . The thermal conductivity of the poly-crystalline Y_2O_3 layer is found to be $k=5.0 \text{ W m}^{-1} \text{ K}^{-1}$, and the conductances of Al/ Y_2O_3 and Y_2O_3 /Si interfaces are $68 \text{ MW m}^{-2} \text{ K}^{-1}$, and $45 \text{ MW m}^{-2} \text{ K}^{-1}$, respectively.

4.2. Introduction

As the feature size of modern electronic devices continues to decrease, the influence of interfaces on heat transfer becomes increasingly important. With layer thicknesses typically in the range of 10's to 100's of nanometers, the interface thermal resistance can

[†] Reprinted with permission from N. C. Shukla, H. H. Liao, J. T. Abiade, F. Liu, P. K. Liaw, and S. T. Huxtable, Applied Physics Letters, 94, 8, 081912, 2009. Copyright 2009, American Institute of Physics.

often dominate over the thermal resistances intrinsic to the layers themselves. In many instances, heat must be transferred from metallic layers to non-metallic layers, thus better understanding of the flow of heat between metals and non-metals would lead to improved thermal management, and enhanced overall performance, in electronic devices.

Electrons dominate heat transport in metals while phonons dominate in non-metal solids. So, there are two possible pathways in which heat could be transported across a metal-nonmetal interface as shown in Fig. 9 (i) direct anharmonic coupling between electrons in the metal and phonons in the nonmetal, or (ii) coupling between electrons and phonons within the metal and then subsequent vibrational coupling across the interface between phonons of the metal and phonons of the nonmetal. The first pathway has been studied only at temperatures less than 1 K [82], while the second has been examined theoretically only recently [9, 48, 53]. Lyeo et al. measured G for interfaces between Bi/dielectrics and Pb/dielectrics, and found that G falls in a narrow range of 8 to 30 MW m⁻² K⁻¹ [9]. It is interesting to note that Pb is a metal while Bi is a semimetal, and they have very similar phonon spectra. Since semi-metals do not have as many electrons as metals, their work seems to indicate that pathway (ii) is more dominant with phonon-phonon coupling across interface being the driving mechanism. However, further work is required in order to fully determine the relative importance of each pathway.

In this work, the thermal conductivity and interface thermal conductance of amorphous and crystalline metallic alloys of Zr₄₇Cu₃₁Al₁₃Ni₉ in contact with polycrystalline Y₂O₃ is studied. By changing the structure, but not the composition, of the alloys one goal of this study is to gain some insight into the role of the metallic lattice on the interface thermal conductance, as well as thermal conductivity, of these materials.

In the amorphous form, metallic alloys are often known as bulk metallic glasses (BMG) and they exhibit great strength, hardness, toughness, corrosion resistance, and elasticity [83-88]. For example, BMG may possess twice the strength to weight ratio of steels, and they are tougher, yet more elastic, than ceramics. Their unique properties have led to the use of BMG in a variety of applications, such as linear actuators, fuel-cell separators, aircraft parts, and sporting goods [89]. In addition to their amorphous glass form, these metallic alloys can often be fabricated in a crystalline form if they are cooled slowly during casting.

4.3. Sample Preparation

The amorphous and crystalline $Zr_{47}Cu_{31}Al_{13}Ni_9$ samples were prepared by Prof. Peter Liaw's group at the University of Tennessee at Knoxville. They are grown by arc-melting a mixture of the constituent metals of Zr, Cu, Al, and Ni (> 99.9% in purity), in a Ti-gettered argon atmosphere. To ensure a homogeneous distribution of the chemical elements, the ingot is melted and flipped three times. The glassy alloy is fabricated using a copper-mold casting method. The amorphous substrates are produced from cylindrical rods that are 4 mm in diameter and 50 mm in length. The crystalline $Zr_{47}Cu_{31}Al_{13}Ni_9$ ingots are melted in the same condition and are cooled slowly. Poly-crystalline Y_2O_3 films are deposited on the metallic alloys by pulsed laser deposition at 400 °C by Prof. Jeremiah Abiade at Virginia Tech.

4.4. Results

The thermal conductivity and interface thermal conductance of the samples are found using time-domain thermoreflectance (TDTR) [5, 70] which is described in detail in chapter 3. The thermal conductivity and interface thermal conductance are extracted simultaneously by comparing the experimental data to a thermal model and adjusting the two parameters until the model matches the data [72]. The inputs to the model include the thickness, heat capacity, and thermal conductivity for each layer in the sample. Interfaces are treated as thin layers (1 nm thick) where the conductance is given by the ratio of the thermal conductivity to the thickness for the layer.

The overall structures of the samples of interest consist of the metallic alloy substrate (~1 mm thick), followed by a Y_2O_3 layer (~95 nm thick) that is coated with a reflective aluminum layer (~80 nm thick). Transmission electron microscopy (TEM) images of the Al/ Y_2O_3 /alloy structures are shown in Fig. 18, and x-ray diffraction (XRD) patterns appear in Fig. 19. The XRD results in Fig. 19 confirm that a poly-crystalline Y_2O_3 layer was deposited on both metallic alloy substrates and that one metallic alloy was amorphous while the other was crystalline. Before the thermal conductivity of the metallic alloy and the conductance of the alloy/ Y_2O_3 interface could be extracted, it is essential to find the thermal conductivity, k , for the Y_2O_3 layer and the interface thermal conductance, G , for the Al/ Y_2O_3 interface by examining a separate reference sample.

Thus, a sample consisting of a silicon wafer coated with poly-crystalline Y_2O_3 (Fig. 19) and aluminum is first prepared. The thermal conductivity of the aluminum is determined to be $k=190 \text{ W m}^{-1} \text{ K}^{-1}$ with four-point probe measurements of the electrical conductivity in conjunction with the Wiedemann-Franz law. Literature values for the

thermal conductivity of Si [90], and the heat capacities of Si [90], Al [91], and Y₂O₃ [92] are used. The thickness of the Al (~82 nm) and Y₂O₃ (~73 nm) layers are found from acoustic echoes [93] with speeds of sound of 6,420 m/s for Al [91], and 7,000 m/s for Y₂O₃ [94, 95]. These thickness measurements are confirmed with transmission electron microscopy. With a laser modulation frequency of $f=9.86$ MHz, we find $k=5$ W m⁻¹ K⁻¹ for the Y₂O₃, $G=68$ MW m⁻² K⁻¹ for the Al/Y₂O₃ interface, and $G=45$ MW m⁻² K⁻¹ for the Y₂O₃/Si interface. The thermal conductivity of the thin Y₂O₃ layer is about a factor of five smaller than a reported value of $k=27$ W m⁻¹ K⁻¹ for a bulk Y₂O₃ crystal [96].

Next, attention is turned back to Al/Y₂O₃/metallic alloy samples. The heat capacity of the Zr₄₇Cu₃₁Al₁₃Ni₉ alloy is calculated to be $C=2.24$ J cm⁻³ K⁻¹ using the Kopp-Neumann law. This calculated value is close to an experimentally determined value [97] of $C=2.28$ J cm⁻³ K⁻¹ for a similar metallic glass, Zr₅₅Cu₃₀Al₁₀Ni₅. In order to confirm these results, and to increase the sensitivity of the measurements, the Al/Y₂O₃/alloy samples are examined at modulation frequencies of $f=9.86$ MHz and $f=4.77$ MHz. Since the penetration depth of the thermal wave is inversely proportional to the square root of the modulation frequency, the lower frequency modulation gives us better sensitivity to the Y₂O₃/alloy interface that is buried deeper in the sample, while the higher frequency measurements allow us to confirm our previous measurements for k of the Y₂O₃ layer and G for the Al/Y₂O₃ interface. Thermorefectance data are shown in Fig. 20 along with “best-fit” curves from the thermal model.

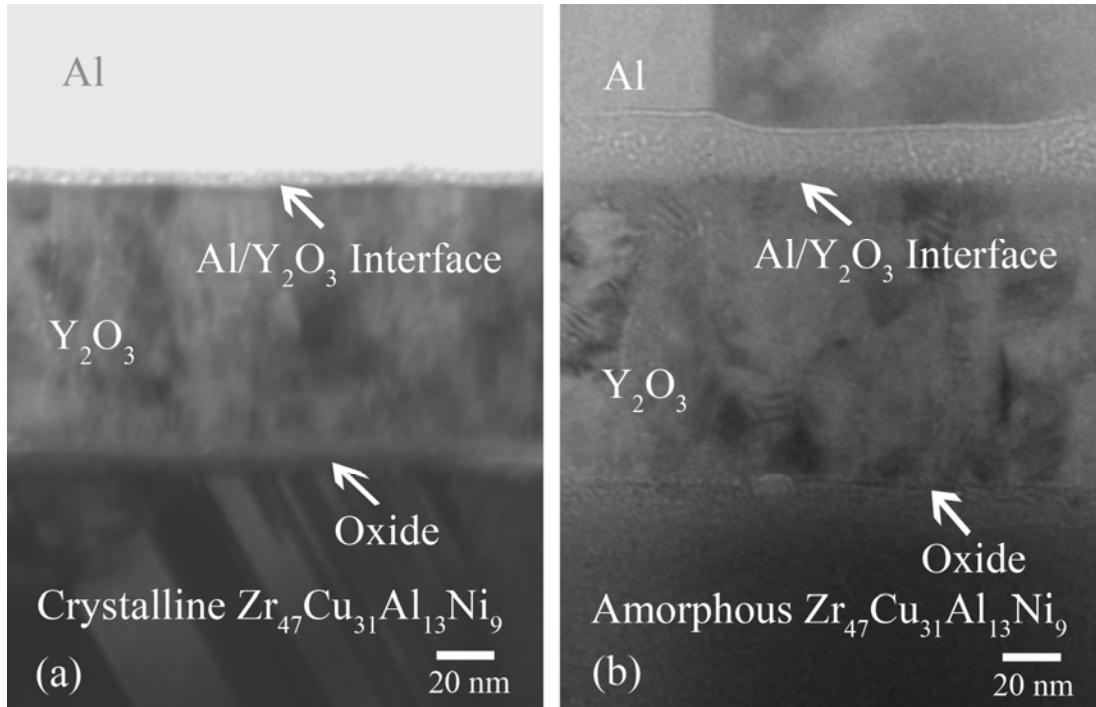


Figure 18: Transmission electron micrographs of (a) crystalline $Zr_{47}Cu_{31}Al_{13}Ni_9$ with Y_2O_3 and Al, and (b) amorphous $Zr_{47}Cu_{31}Al_{13}Ni_9$ with Y_2O_3 and Al. Note the presence of a ~ 5 nm thick oxide layer on the surface of metallic alloy layers. The lack of structure in the Al layer and the blurriness of the entire image in (a) is an artifact due to the unfortunately large thickness of the TEM specimen. The TEM specimen for sample (b) is considerably thinner, thus the image is sharper. The change in structure in the Al layer in (b) after ~ 20 nm is likely due to a sudden change in the deposition rate of the Al during electron beam evaporation. The two blocks at the top of the Al layer are crystallites. Energy dispersive x-ray spectroscopy (EDX) analyses on both aluminum layers confirm that the entire layers are essentially pure aluminum. The change in structure of the aluminum throughout the layer should have minimal effect on the results since the heat capacity and thermal conductivity of aluminum are not significantly influenced by these changes in morphology.

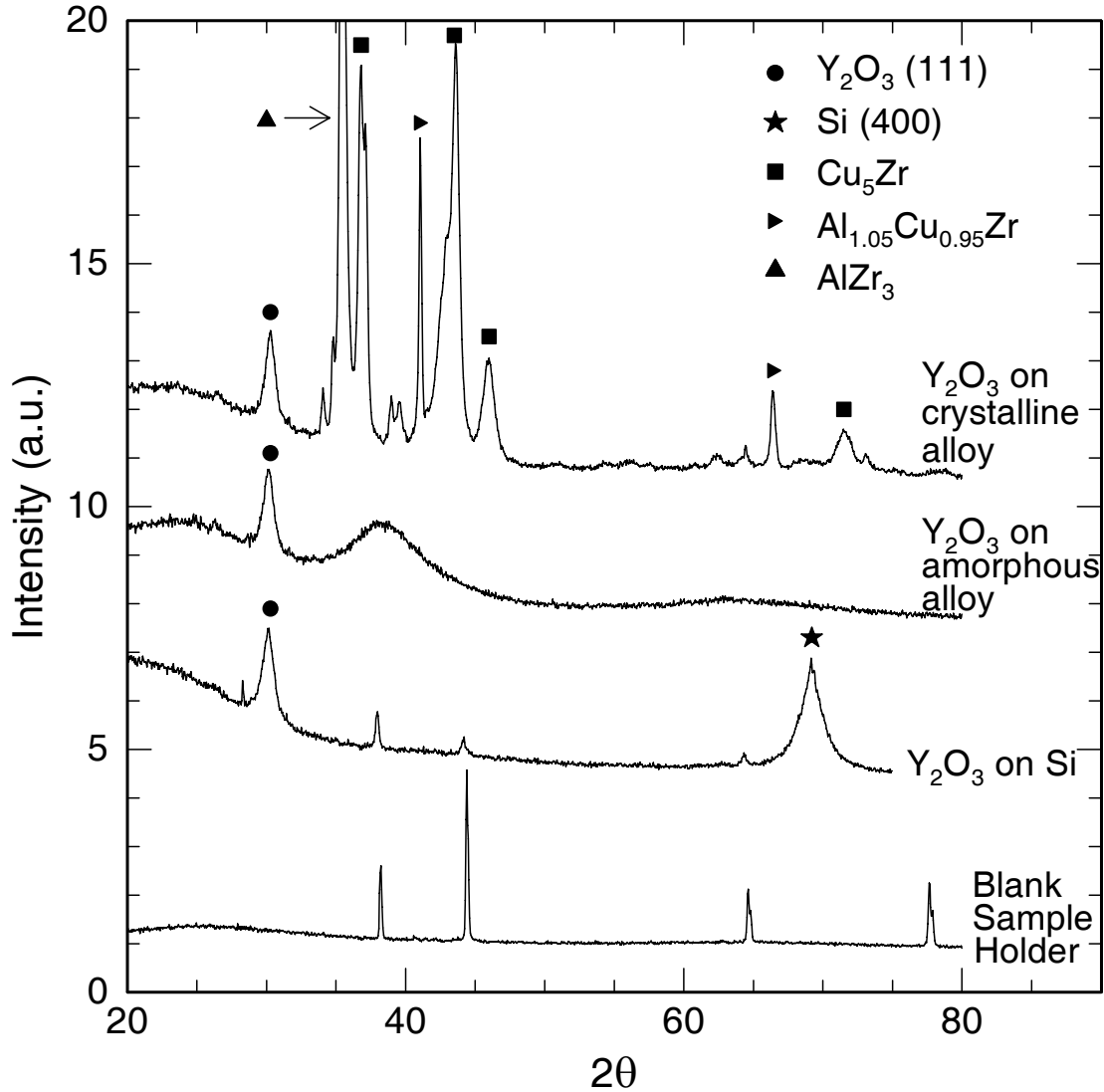


Figure 19: X-ray diffraction (XRD) patterns for Y_2O_3 , amorphous and crystalline $Zr_{47}Cu_{31}Al_{13}Ni_9$ alloys, and Si. The XRD patterns are obtained using K-alpha emission from copper with a wavelength of 1.5406 Å. The sharp peaks for Y_2O_3 and one alloy indicate that the materials are partially crystalline, while the broad peak for the second alloy demonstrates that it is amorphous. The labels on the plot refer to peaks that are matched with materials in the Powder Diffraction File database (PDF). The sharp peaks that appear in the blank sample holder are partially attenuated in the Y_2O_3 on Si sample, and fully attenuated in the metallic alloy samples due to the increased thickness of these samples.

The TDTR measurements give $k=4.5 \text{ W m}^{-1} \text{ K}^{-1}$ for the amorphous alloy, and $k=5.0 \text{ W m}^{-1} \text{ K}^{-1}$ for the crystalline alloy. These thermal conductivity values are similar to those reported by Yamasaki and coworkers for amorphous $\text{Zr}_{55}\text{Al}_{10}\text{Ni}_5\text{Cu}_{30}$ (Ref. [97], $5.0 \text{ W m}^{-1} \text{ K}^{-1}$) and for amorphous $\text{Zr}_{41}\text{Ti}_{14}\text{Cu}_{12}\text{Ni}_{10}\text{Be}_{23}$ (Ref. [98], $4.6 \text{ W m}^{-1} \text{ K}^{-1}$). The electronic contribution, k_e , to each thermal conductivity value can be estimated by again using the Wiedemann-Franz law in conjunction with the Van der Pauw method [99] for electrical conductivity measurements.

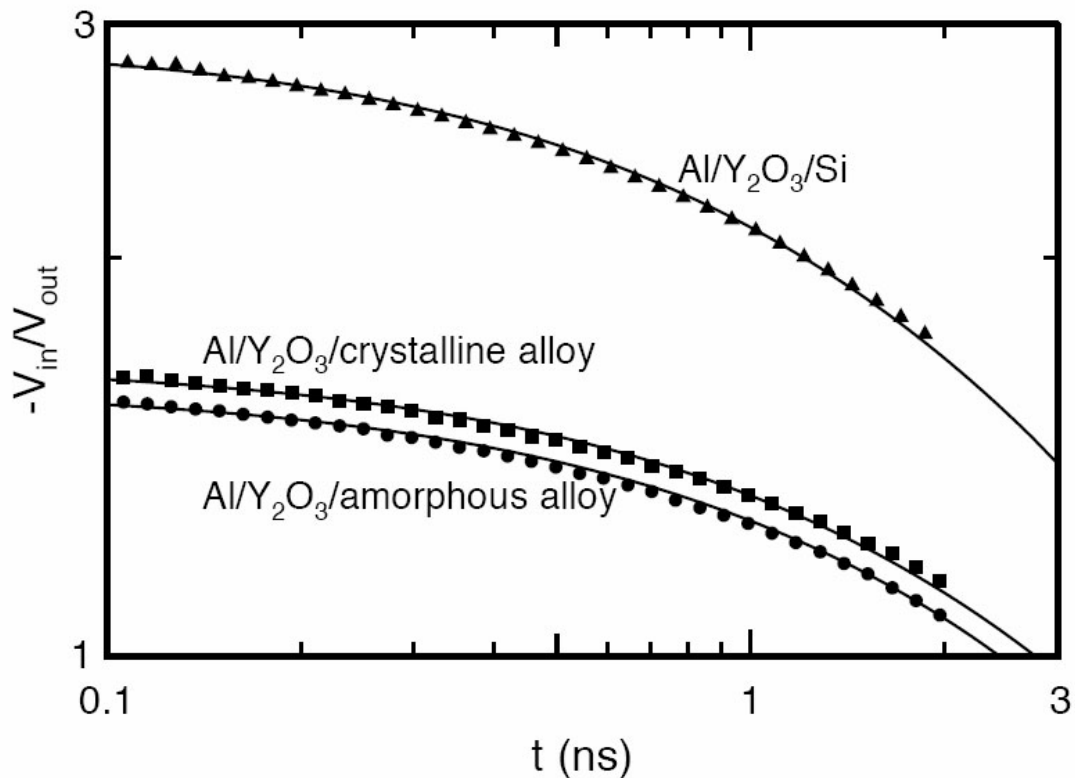


Figure 20: Time-domain thermoreflectance data (TDTR) on the $\text{Al}/\text{Y}_2\text{O}_3/\text{alloys}$ and the $\text{Al}/\text{Y}_2\text{O}_3/\text{Si}$ sample. “ $V_{\text{in}}/V_{\text{out}}$ ” represents the ratio of the in-phase/out-of-phase voltage as measured by a lock-in amplifier. The data taken on the $\text{Al}/\text{Y}_2\text{O}_3/\text{Si}$ sample (\blacktriangle) are used to find the conductivity of the Y_2O_3 layer as well as the conductance of the $\text{Al}/\text{Y}_2\text{O}_3$ and $\text{Y}_2\text{O}_3/\text{Si}$ interfaces. The measurements on the crystalline (\blacksquare) and amorphous (\bullet) alloys give the conductivity of each alloy along with the conductance of each $\text{Y}_2\text{O}_3/\text{alloy}$ interface. The solid lines represent the “best-fit” from the thermal model. The models all used identical material properties for Al, the $\text{Al}/\text{Y}_2\text{O}_3$ interface, and the Y_2O_3 layer.

The Van der Pauw method is a four point probe technique for measuring the sheet resistance of a flat structure and is widely used in the integrated circuit industry for measuring electrical conductivity. The Van der Pauw method is employed because our samples are small and of arbitrary shape, and this method is effective even for such structures. The four probes are placed along the periphery of the sample as shown in Fig. 21. Next, a current I_{12} is passed from connection 1 to connection 2, and the voltage $V_{34}=V_3-V_4$ is measured using a digital multimeter. The resistance $R_{12,34}$ is then defined as $R_{12,34}=\frac{V_{34}}{I_{12}}$. Similarly, $R_{23,41}$ is also defined and measured. The electrical resistivity is

calculated by using following equation:

$$\rho_s = \frac{\pi}{\ln(2)} \frac{(R_{12,34} + R_{23,41})}{2} F \quad (4.1)$$

where t is the thickness of sample, and F is a correction factor which is a function of the ratio $(R_{12,34}/R_{12,34})$. This correction factor may be found in literature (Reference [99], Page 15).

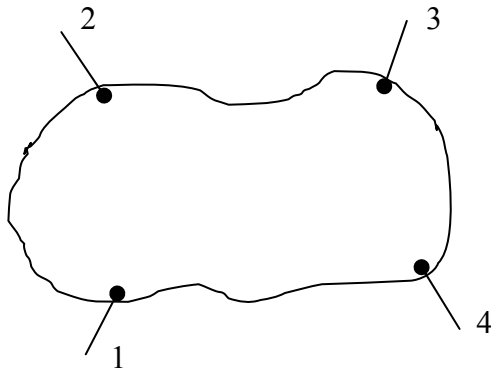


Figure 21: Schematic diagram of the Van der Pauw method for an arbitrarily shaped flat structure. The four probes are randomly placed on the periphery of the structure.

The Van der Pauw measurements in conjunction with the Wiedemann-Franz law give $k_e=3.75 \text{ W m}^{-1} \text{ K}^{-1}$ for the amorphous alloy and $k_e=4.0 \text{ W m}^{-1} \text{ K}^{-1}$ for the crystalline alloy, which leaves lattice (phonon) components, k_p , of the thermal conductivity of $k_p=0.75 \text{ W m}^{-1} \text{ K}^{-1}$ for the amorphous alloy and $k_p=1.0 \text{ W m}^{-1} \text{ K}^{-1}$ for the crystalline alloy.

The "minimum lattice thermal conductivity" [100-102] model is used to predict the minimum lattice thermal conductivity of BMG. The minimum thermal conductivity, k_{min} , of a bulk solid is defined as the thermal conductivity of the solid if it were completely amorphous in nature. The mean free path of phonons at room temperature for amorphous solids is on the order of phonon wavelength [103, 104]. Therefore, this model assumes that lattice vibrations may be described as localized oscillators as proposed by Einstein [100], rather than assuming them as waves. These oscillators are coupled to their nearest neighbors and the energy is transported through a random walk between oscillators. By combining the assumptions borrowed from Einstein's and Debye models, Cahill and Pohl derived the following relation for minimum conductivity [105]:

$$k_{min} = \left(\frac{\pi}{6}\right)^{1/3} k_B n^{2/3} \sum_i v_i \left(\frac{T}{\theta_i}\right)^2 \int_0^{\theta_i} \frac{x^3 e^x}{(e^x - 1)^2} dx \quad (4.2)$$

where v_i represents speed of sound in i th direction, $\theta_i = v_i(h/k_B)(6\pi^2 n)^{1/3}$ is the cutoff frequency for each polarization expressed in degree K, and n is the number density of atoms, h is the Planck's constant and k_B is Boltzmann's constant. The summation is taken over all three polarization states (one longitudinal and two transverse modes). As elastic property data is not yet available for $\text{Zr}_{47}\text{Cu}_{31}\text{Al}_{13}\text{Ni}_9$ alloy, we calculate the "minimum lattice thermal conductivity" using material properties for a similar ($\text{Zr}_{55}\text{Cu}_{30}\text{Al}_{10}\text{Ni}_5$) BMG [106] and find $k_{min}=0.6 \text{ W m}^{-1} \text{ K}^{-1}$. This value of k_{min} is comparable to the lattice

thermal conductivity for amorphous and crystalline $Zr_{47}Cu_{31}Al_{13}Ni_9$ alloy, suggesting a large degree of disorder in their structure.

Finally, the interface thermal conductance between the alloy and the Y_2O_3 layer is extracted and found to be $G=23 \text{ MW m}^{-2} \text{ K}^{-1}$ for the amorphous alloy/ Y_2O_3 interface and $G=26 \text{ MW m}^{-2} \text{ K}^{-1}$ for the crystalline alloy/ Y_2O_3 interface. It is also worth mentioning here that there is a $\sim 5 \text{ nm}$ thick oxide layer present at the alloy/ Y_2O_3 interfaces as is typical of Zr-based BMG [107]. Thus, the reported interface conductance is really the sum of the interface conductance between the Y_2O_3 and the oxide, the conductance of the oxide layer itself, and the interface conductance between the oxide and the metallic alloy. However, assuming a typical oxide conductivity of $1 \text{ W m}^{-1} \text{ K}^{-1}$ for this layer, the oxide layer itself would only contribute $\sim 12\%$ of the total thermal resistance of the interface. Thus, the transfer of energy between the metal and non-metal dominates the measured interface conductance.

Despite the small difference between k and G for the two alloys, the results are repeatable and they indicate that the structure of the alloy plays a role in the electron-phonon coupling and interface conductance. While part of the motivation for this study was to examine the effect of the alloy structure on the interface conductance, it is difficult to draw solid conclusions about the precise role of electron-phonon or phonon-phonon coupling at the interface due to the small separation in the lattice components of the thermal conductivity of the amorphous and crystalline layers. Future work will focus on materials that possess a larger difference in lattice thermal conductivity between crystalline and amorphous structures.

5. Thermal transport in composites of self-assembled nickel nanoparticles embedded in yttria stabilized zirconia[‡]

5.1. Abstract

This chapter investigates the effect of nickel nanoparticle size on thermal transport in multilayer nanocomposites consisting of alternating layers of nickel nanoparticles and yttria stabilized zirconia (YSZ) spacer layers that are grown with pulsed laser deposition. The time-domain thermorefectance measures thermal conductivities of $k=1.8, 2.4, 2.3,$ and $3.0 \text{ W m}^{-1} \text{ K}^{-1}$ for nanocomposites with nickel nanoparticle diameters of 7, 21, 24, and 38 nm, respectively, and $k=2.5 \text{ W m}^{-1} \text{ K}^{-1}$ for a single 80 nm thick layer of YSZ. An effective medium theory is used to estimate the lower limits for interface thermal conductance, G , between the nickel nanoparticles and the YSZ matrix ($G>170 \text{ MW m}^{-2} \text{ K}^{-1}$), and nickel nanoparticle thermal conductivity.

5.2. Introduction

Materials composed of self-assembled nanoparticles embedded in a matrix material exhibit interesting physical properties. The inclusion of nanoparticles in composite materials may result in unique or improved mechanical, optical, electrical, thermal, and magnetic properties [83, 108, 109]. These composite materials may find potential applications in data storage devices, biochemical sensors, magnetic field sensors, and

[‡] Reprinted with permission from N. C. Shukla, H. H. Liao, J. T. Abiade, M. Murayama, D. Kumar, and S. T. Huxtable, Applied Physics Letters, 94, 15, 15193, 2009. Copyright 2009, American Institute of Physics.

single electron devices [110, 111]. This chapter examines the effect of nanoparticle size on thermal transport in a series of nanocomposites that consist of layers of nickel nanoparticles embedded in a yttria stabilized zirconia (YSZ) matrix. A better understanding of heat transport in nanostructured composite materials is important not only from a scientific viewpoint but also to improve the performance of many of the above-mentioned devices.

5.3. Sample preparation

The Ni/YSZ composites were fabricated by Prof. Jeremiah Abiade. Nickel nanoparticles are embedded in poly-crystalline YSZ films by laser ablation of Ni and YSZ (5 weight% yttria) targets using pulsed laser deposition (PLD) [112]. To avoid the formation of NiO or Ni/NiO core/shell structures, oxygen is not used and the depositions are done in vacuum ($\sim 5 \times 10^{-7}$ Torr). The final structure of the multi-layered nanocomposites consists of an initial YSZ buffer layer (~ 100 nm) followed by five Ni nanoparticle layers (7-38 nm) that are separated by four YSZ spacer layers (22-48 nm) as shown in Fig. 22. The Ni particle size is altered by varying the number of laser pulses at a laser frequency of 10 Hz.

Microstructural investigations are carried out using an FEI TITAN 80-300 Transmission Electron Microscope (TEM) at the Virginia Tech Institute for Critical Technologies and Applied Science. The TEM is equipped with an E.A. Fischione model 3000 annular dark field detector, and it is operated at 200kV in Scanning Transmission Electron Microscopy (STEM) mode. The size of the electron probe is approximately 1 nm in diameter. STEM dark field images of these four samples (see Fig. 22) determines

the average Ni nanoparticle diameters to be approximately 7, 21, 24, and 38 nm for samples 1-4, respectively. While these particular samples were not analyzed with Electron Energy Loss Spectroscopy (EELS), similar samples grown by the same group were examined with EELS and pure metallic Ni nanoparticles without oxide layers were found [113].

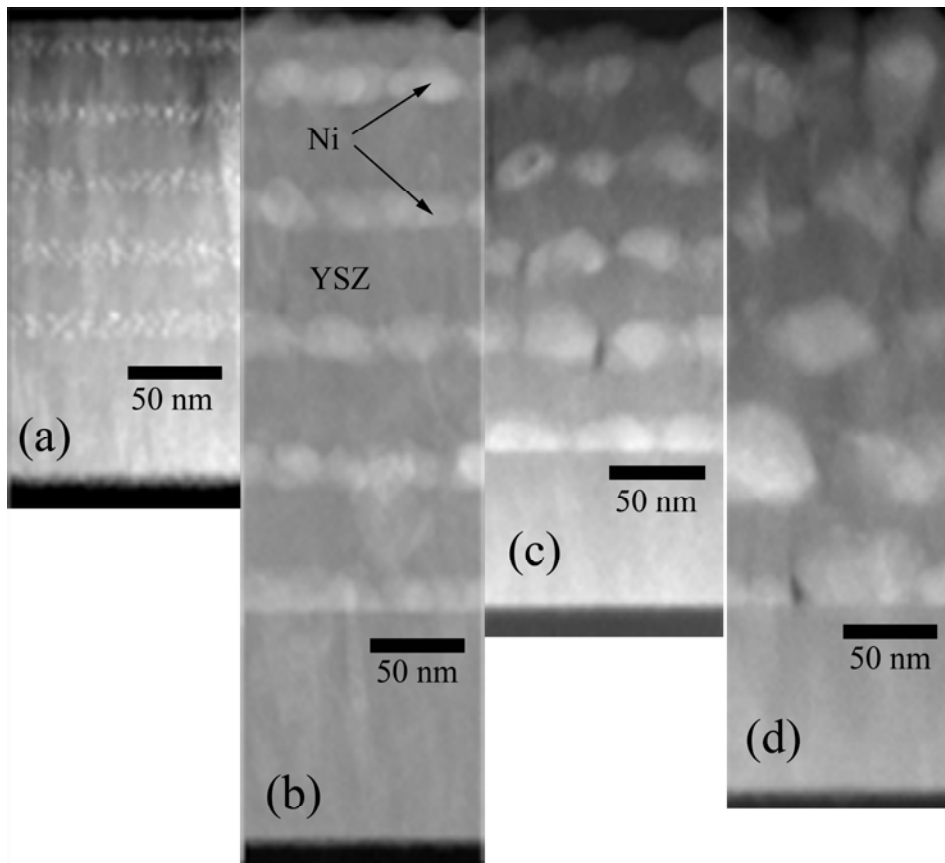


Figure 22: Scanning transmission electron micrographs of the Ni/YSZ nanocomposites. Each sample consists of five layers of Ni nanoparticles separated by four YSZ spacer layers and they are grown on Si substrates with YSZ buffer and cap layers. The dimensions of the samples are given in Table 5. Images (a)-(d) correspond to samples 1-4, respectively.

5.4. Results

A time-domain thermoreflectance (TDTR) system is used to measure the thermal conductivity, k , and interface thermal conductance, G , of the nanocomposites. TDTR is a pump-probe optical technique that takes advantage of the fact that the reflectivity of a metal has a slight dependence on temperature. The $1/e^2$ beam diameters at the sample are 30 μm for the pump beam and 18 μm for the probe beam. Data are recorded with a lock-in amplifier in order to improve the signal-to-noise ratio.

The ratio of the in-phase voltage to the out-of-phase voltage measured by the lock-in amplifier is compared with a one dimensional heat transfer model for multilayer structures to extract thermal conductivity and interface thermal conductance. Since the TDTR model is valid only for layers of uniform thickness, we represent the Ni nanoparticle layer as a Ni/YSZ composite layer with the layer thickness set equal to the diameter of the Ni nanoparticles as shown in Fig. 23. This Ni/YSZ composite layer is approximated as a layer of uniformly arranged spherical Ni nanoparticles surrounded by YSZ. Thus the overall structure in the model consists of alternating Ni/YSZ composite layers separated by YSZ spacer layers. For spherical nanoparticles, the maximum volume fraction within the Ni/YSZ composite layer is given by the case where each nanoparticle is touching four neighboring Ni nanoparticles and the volume fraction, f , of Ni in YSZ is then $f=\pi/6$, or $\sim 52.4\%$.

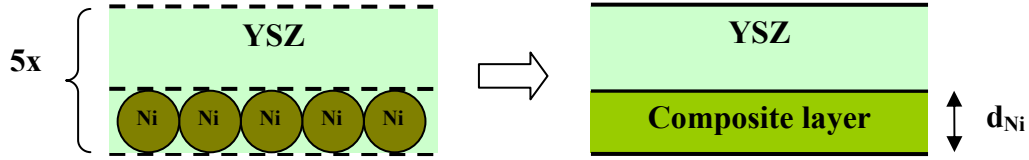


Figure 23: TDTR modeling for each period of nanocomposite. Each period consists of the YSZ spacer and Ni nanoparticle layers. The Ni particle layer may be considered as a composite layer that contains $\pi/6$ volume fraction of Ni and $(1-\pi/6)$ fraction of YSZ. The heat capacity of this composite layer is calculated by taking the volumetric weighted average of Ni and YSZ components in the layer.

The TDTR model requires thickness, heat capacity, and thermal conductivity of each layer, along with the interface thermal conductance between the layers in our nanocomposite structure, as input parameters. The thickness of aluminum layer is calculated using measurements of the acoustic echoes [93] with the speed of sound for Al taken as 6420 m/s [91]. The YSZ and Ni/YSZ composite layer thicknesses are measured using the TEM. The heat capacities of Al, Ni, and Si are taken from literature values [90, 91] while the heat capacity of YSZ is calculated using literature values for the constituent materials Y_2O_3 [92] and ZrO_2 [114]. The heat capacity of the Ni/YSZ composite layer is then calculated using the Kopp-Neumann law assuming the volume fraction of Ni to be $\pi/6$. It is worthwhile to point out that the uncertainty in the heat capacity of the Ni/YSZ composite layer resulting from uncertainty in the Ni volume fraction does not strongly influence the TDTR measurement results. For example, a 25% change in the Ni volume fraction in the TDTR model results in a change of less than 8% in the measured thermal conductivity of the Ni/YSZ composite layer. The thermal conductivity of silicon is taken from Shanks et al. [90], and the thermal conductivity of the aluminum layer is found to be $185 \text{ W m}^{-1} \text{ K}^{-1}$ using four-point probe electrical conductivity measurements in conjunction with the Wiedemann-Franz law.

Thus, the only unknown parameters in our TDTR model are: G between Al and YSZ, k of YSZ, and the effective k of the Ni/YSZ composite layer. This effective k includes the interface thermal conductance between the Ni nanoparticles and the YSZ matrix, which is discussed later. In order to reduce the number of unknown parameters, k for YSZ and G between Al and YSZ are first measured by preparing a reference sample that consists of 80 nm of YSZ deposited on a Si substrate. TDTR finds $k=2.5 \text{ W m}^{-1} \text{ K}^{-1}$ for YSZ and $G=100 \text{ MW m}^{-2} \text{ K}^{-1}$ for the Al/YSZ interface. This experimental value of k for YSZ is similar to values of 2.3-3.0 $\text{W m}^{-1} \text{ K}^{-1}$ reported in the literature [115, 116].

Next, the above values are used to extract the effective k for the Ni/YSZ composite layers and we find k to be 1.3, 2.2, 2.1, and 3.5 $\text{W m}^{-1} \text{ K}^{-1}$ in samples 1-4, respectively. In order to determine the overall thermal conductivity of the entire nine layer structure, a simple series thermal resistance model is created that consists of the five Ni/YSZ composite layers in series with the four YSZ spacer layers.

By dividing the total thickness of the nine layers by the total thermal resistance of the same layers, the overall thermal conductivities of the entire multilayer structures is found to be 1.8, 2.4, 2.3, and 3.0 $\text{W m}^{-1} \text{ K}^{-1}$ for samples 1-4, respectively (see Table 5). Since the thermal conductivity of bulk nickel is $\sim 90 \text{ W m}^{-1} \text{ K}^{-1}$ [91], thermal models that ignore interface effects would predict an increase in the thermal conductivity with the addition of a higher thermal conductivity material in a low thermal conductivity matrix. However, a decrease in the thermal conductivity is observed for samples 1, 2, and 3 that contain smaller nanoparticles. This decrease in thermal conductivity indicates that the interface thermal resistance between YSZ and Ni becomes dominant at these lengthscales

and/or the thermal conductivity of the nickel becomes comparatively low for these nanoparticles. We address these two possibilities below.

With the use of an effective medium theory [117-119], in principle one could estimate G or k for the nanoparticles within these types of composite materials. In this particular instance, uncertainty in the Ni volume fraction makes it difficult to extract specific values for either G or k for the nanoparticle. However, with an estimate of the Ni volume fraction we can place approximate lower bounds on both properties through the use of an effective medium theory.

Table 5: Summary of properties for each sample. The effective thermal conductivity of the Ni/YSZ composite layers is extracted with TDTR. The overall thermal conductivity of the nanocomposite is calculated using a series thermal model in conjunction with our measurements on YSZ and the Ni/YSZ composite layers.

Sample	Diameter of Ni nanoparticles (nm)	Thickness of YSZ spacer (nm)	Effective k of Ni/YSZ composite layer ($\text{W m}^{-1} \text{K}^{-1}$)	Overall k of nanocomposite structure ($\text{W m}^{-1} \text{K}^{-1}$)
1	7	22	1.3	1.8
2	21	48	2.2	2.4
3	24	22	2.1	2.3
4	38	28	3.5	3.0

Every et al. [119] developed the following equation for composites made from spherical particles embedded in a host matrix that relates the thermal conductivity of the composite, k_c , to the thermal conductivity of the host matrix, k_m , the thermal conductivity of a spherical particle, k_p , the interface thermal conductance, G , between the particle and the matrix, the radius of the particle, r_p , and the volume fraction, f , of the particles for the high volume fraction limit:

$$(1-f)^3 = \left(\frac{k_m}{k_c}\right)^{\frac{1+2\alpha}{1-\alpha}} \times \left\{ \frac{k_c - k_p(1-\alpha)}{k_m - k_p(1-\alpha)} \right\}^{\frac{3}{1-\alpha}} \quad (5.1)$$

where $\alpha = \frac{k_m}{r_p G}$.

For $f=\pi/6$, we plot the Ni/YSZ interface thermal conductance as a function of the thermal conductivity of the Ni nanoparticles k_p for all four samples in Fig. 24. This plot demonstrates two interesting features. First, it is found that the Ni/YSZ interface thermal conductance decreases with increasing k_p , but approaches a minimum value for $k_p > 20 \text{ W m}^{-1} \text{ K}^{-1}$ for all four samples. In other words, the thermal resistance at the Ni/YSZ interface dominates if $k_p > 20 \text{ W m}^{-1} \text{ K}^{-1}$. It is illuminating to point out that recent molecular dynamics simulations [120] predict that the thermal conductivity of nickel nanoparticles will always be above $30 \text{ W m}^{-1} \text{ K}^{-1}$ for nanoparticles greater than 7 nm in diameter. These results illustrate the critical importance of the interface if one intends to enhance the thermal conductivity of a composite material by introducing high conductivity particles. The effective medium theory also allows us to place an approximate lower bound on G of 170-210 MW m⁻² K⁻¹ for the four samples, which falls in the middle of the typical range of $80 < G < 300 \text{ MW m}^{-2} \text{ K}^{-1}$ [51] for many phonon-mediated interfaces. Gundrum et al. [51] measured G to be $\sim 250 \text{ MW m}^{-2} \text{ K}^{-1}$ for a similar metal-nonmetal interface between Cu and Al₂O₃.

Alternatively, by assigning an upper bound on G , we can estimate a lower limit for the Ni nanoparticle thermal conductivity. From the literature [51], the majority of metal/dielectric interfaces have $G < 300 \text{ MW m}^{-2} \text{ K}^{-1}$ (with one notable exception [49] of $G \sim 700 \text{ MW m}^{-2} \text{ K}^{-1}$ for TiN/MgO [49]). Taking $G=300 \text{ MW m}^{-2} \text{ K}^{-1}$, we find the minimum values of k_p to be 1.6, 5.8, 3.9, and 15.8 W m⁻¹ K⁻¹ for Ni nanoparticles with

diameters of 7, 21, 24, and 38 nm, respectively (see Fig. 24). Given that these minimum thermal conductivity values are much smaller than estimates from molecular dynamics simulations [120], it seems likely that the actual Ni/YSZ interface conductance is closer to the lower limit of $\sim 200 \text{ MW m}^{-2} \text{ K}^{-1}$.

Interface thermal conductance between Ni and YSZ matrix may be predicted using the acoustic mismatch model (AMM) described in chapter 2. Swartz and Pohl [37] developed a relation for interface thermal conductance:

$$G = \frac{1}{4} \rho C v \eta, \quad (5.2)$$

where ρ is the density, C is the specific heat and v is the Debye velocity of the matrix and η is the transmission probability for phonons. The fraction q of the incident phonons that may fall within θ_c is given by [119]:

$$q = \frac{1}{2} \sin^2 \theta_c = \frac{1}{2} \left(\frac{v_1}{v_2} \right)^2, \quad (5.3)$$

where v_1 and v_2 are the speed of sound in YSZ and Ni, respectively. Assuming $v_1 \approx 3000$ m/s [121] and $v_2 \approx 3700$ m/s [122], we calculate $q = 0.33$. Now, the probability, $T_{\text{YSZ} \rightarrow \text{Ni}}$, that an incident phonon from the YSZ side is transmitted to the Ni side is given by

equation (2.8): $T_{\text{YSZ} \rightarrow \text{Ni}} = \frac{4Z_{\text{YSZ}}Z_{\text{Ni}}}{(Z_{\text{YSZ}} + Z_{\text{Ni}})^2}$. Using densities for YSZ and Ni from the literature

[95, 122], we calculate acoustic impedances of $Z_{\text{YSZ}} = 1.8 \times 10^7 \text{ Kg m}^{-2} \text{ s}^{-1}$ and $Z_{\text{Ni}} = 3.3 \times 10^7 \text{ Kg m}^{-2} \text{ s}^{-1}$, and $T_{\text{YSZ} \rightarrow \text{Ni}} = 0.91$. The transmission probability for phonons is then calculated

as $\eta = q * T_{\text{YSZ} \rightarrow \text{Ni}} = 0.3$. Finally, we calculate $G = \frac{1}{4} \rho C v \eta = \frac{1}{4} (8980)(500)(6000)(0.3) = 676 \text{ MW}$

$\text{m}^{-2} \text{ K}^{-1}$ using equation (5.2). The factor of ~ 3 difference between the measured value and

the AMM prediction is expected since the AMM does not include the dispersion effects and the model typically overestimates experiments by a factor of 2-4.

In summary, the thermal transport in nanocomposites composed of Ni nanoparticles embedded in a YSZ matrix is investigated. The Ni nanoparticle size and interface thermal conductance strongly influence the overall thermal conductivity of these nanocomposites. For small nanoparticles with diameters between 7 and 24 nm, the inclusion of the nanoparticles decreases the thermal conductivity of the composite, while 38 nm diameter particles increase the thermal conductivity of the composite. An effective medium theory is used to place an approximate lower bound of $170 \text{ MW m}^{-2} \text{ K}^{-1}$ on the Ni/YSZ interface thermal conductance.

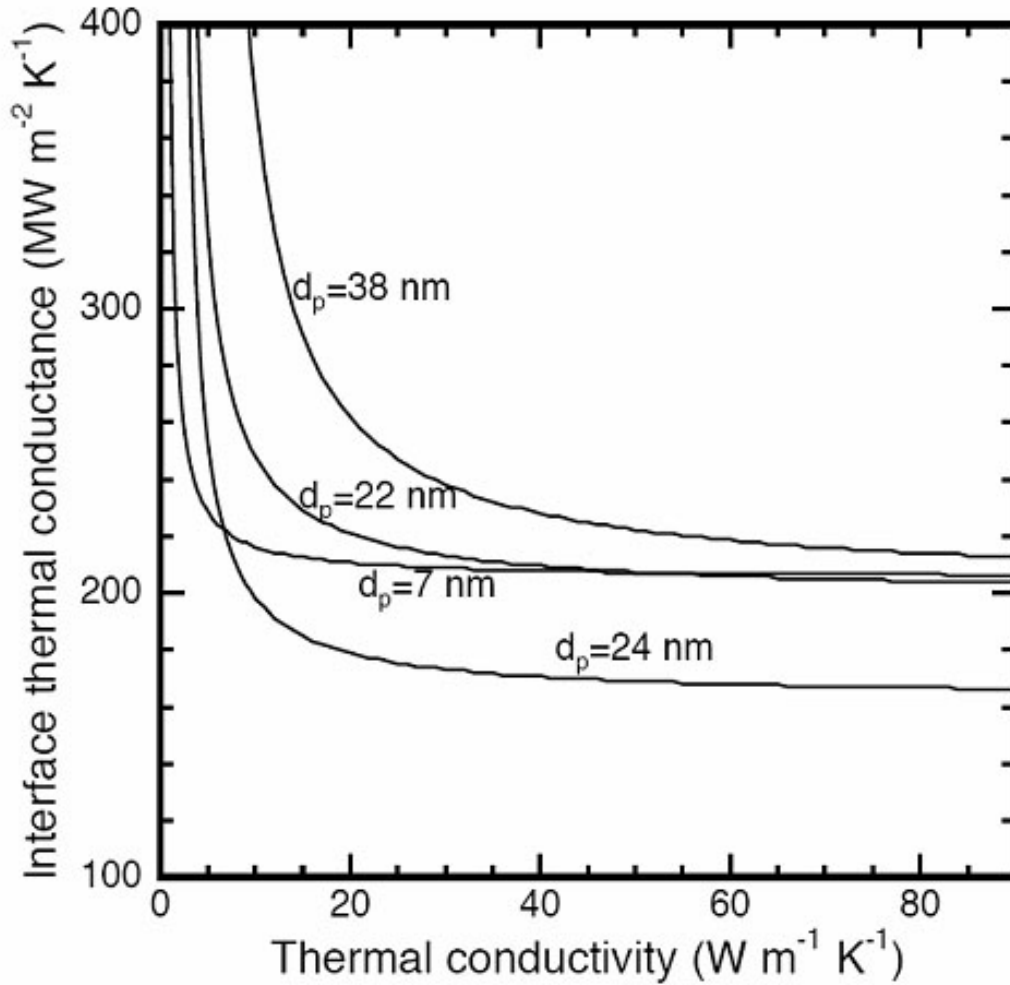


Figure 24: Interface thermal conductance between the Ni nanoparticles and the surrounding YSZ matrix as a function of Ni nanoparticle thermal conductivity. The solid lines are predictions from an effective medium theory for each sample with a Ni volume fraction of $f=\pi/6$. The labels on the plot refer to the average diameter of the nickel nanoparticles in each sample. We find a lower limit for the Ni/YSZ interface thermal conductance of ~ 170 MW m⁻² K⁻¹.

6. Conclusions and Future Work

The physics of the interface thermal conductance between solid-solid materials is only partially understood. A more complete understanding of such interfaces is critical in designing and improving the performance of a wide variety of devices and materials including microelectronics, thermoelectrics, heat spreaders, thermal insulators, and composites. This dissertation is aimed at developing better insight into the heat transport mechanisms across metal-nonmetal interfaces. A time-domain thermoreflectance (TDTR) experimental technique is used to measure the thermal conductivity and interface thermal conductance of metallic alloys and nanocomposite materials. In this chapter, conclusions and directions for future work are presented.

In chapter 4, the thermal properties of amorphous $Zr_{47}Cu_{31}Al_{13}Ni_9$, crystalline $Zr_{47}Cu_{31}Al_{13}Ni_9$, and thin a Y_2O_3 film were measured using a TDTR method. The thermal conductivities of amorphous $Zr_{47}Cu_{31}Al_{13}Ni_9$, crystalline $Zr_{47}Cu_{31}Al_{13}Ni_9$, and thin poly-crystalline Y_2O_3 film are found to be 4.5, 5.0, and 5.0 $W m^{-1} K^{-1}$, respectively. This phonon contributions to thermal conductivity are determined to be 0.75 $W m^{-1} K^{-1}$ and 1.0 $W m^{-1} K^{-1}$ for the amorphous and crystalline metallic alloys, respectively. The thermal conductances for the interfaces between the amorphous and crystalline $Zr_{47}Cu_{31}Al_{13}Ni_9$ with Y_2O_3 are measured to be 23 and 26 $MW m^{-2} K^{-1}$, respectively. These values of interface thermal conductance fall in the typical range of 8-300 $MW m^{-2} K^{-1}$ for solid-solid interfaces.

Despite the apparent small difference between k and G for the amorphous and crystalline $Zr_{47}Cu_{31}Al_{13}Ni_9$ metal alloys, there is a noticeable and reproducible change in

thermal behavior in the two materials. Thus, this is the one of the first experimental studies to isolate the effect of structure apart from composition of an alloy and to quantitatively show that the structure of an alloy plays a measurable role in the interface conductance between metals and nonmetals.

In chapter 5, the effect of Ni nanoparticle size on the overall thermal properties of nanocomposites is studied. These nanocomposites consist of five alternating layers of Ni nanoparticles embedded in a YSZ matrix. TDTR measures thermal conductivities of the nanocomposites to be 1.8, 2.4, 2.3, and 3.0 for Ni particle diameters of 7, 21, 24, and 38 nm, respectively. TDTR also determines the thermal conductivity of YSZ to be $2.5 \text{ W m}^{-1} \text{ K}^{-1}$.

It is interesting to note a reduction in the thermal conductivity of nanocomposites compared to the matrix material for smaller Ni nanoparticles of diameters 7, 21, and 24 nm. This suggests either of the following possibilities: (i) the thermal conductivity of the Ni nanoparticles is smaller compared to YSZ matrix, (ii) the interface thermal conductance between the Ni nanoparticles and YSZ becomes dominant, or (iii) a combination of (i) and (ii).

Effective medium theory is used to examine the relation between the thermal conductivity of the Ni particles and the interface thermal conductance between Ni and YSZ. For a Ni volume fraction of $\pi/6$, it is found that the interface conductance approaches a minimum value of $\sim 200 \text{ MW m}^{-2} \text{ K}^{-1}$ for all four samples if $k_{\text{Ni}} > 30 \text{ W m}^{-1} \text{ K}^{-1}$. This value of interface thermal conductance is typical of a metal/nonmetal interface. The importance of these values of interface conductance becomes more significant when we consider the molecular dynamics simulations conducted on Ni nanoparticles by Yuan

and Jiang [120]. It was shown in their work that for Ni particle sizes of 7 nm and larger, k_{Ni} would always be larger than $30 \text{ W m}^{-1} \text{ K}^{-1}$. In light of their results, it seems unlikely that the reduction in thermal conductivity of the composites was caused by a reduction of conductivity within the Ni nanoparticles. It is much more plausible that the interface resistance was the key factor in reducing the thermal conductivity of the small diameter nanocomposites. This is the one of the first experimental studies to approximate the interface thermal conductance between a nanoparticle and a surrounding matrix.

6.1. Future directions

The future research should look into metallic alloys that have wider separation in lattice thermal conductivities of amorphous and crystalline forms. This will help further determine the relative importance of the two pathways for interface conductance discussed in chapter 4. Liquid metals also present an interesting case for investigating metal/nonmetal interfaces. In liquid form, the phonon component to heat transport will be significantly reduced. Measurements of interface thermal conductance as a function of temperature across the melting point will provide an excellent way to probe electron-phonon coupling across the interface. Gallium and indium are metals with relatively low melting points of ~ 30 and $155 \text{ }^\circ\text{C}$, respectively, and would be excellent candidate materials to examine. However, the experimental realization of such liquid metal samples will be a difficult task due to the following reasons: (i) difficulty in depositing such metals due to their high vapor pressure, and (ii) designing a heating setup that ensures that the metal when melted remains in intimate contact with the nonmetal side.

It will also be interesting to measure the interface conductance between planar layers of Ni and YSZ. With independent measurements of the Ni/YSZ interface conductance, one could extract the thermal conductivity of the Ni nanoparticles using the analysis outlined in Chapter 5. It would be interesting to compare the thermal conductivity of thin metal films with the conductivity of the same metals in nanoparticle form. In nanoparticles embedded in a matrix, the energy carriers are confined in three dimensions, while in the planar case they are confined only in one direction. It will be of great scientific importance to examine the effect of dimensional confinement on the thermal conductivity of these nanoparticles.

Appendix A

The following is the Fortran code for one-dimensional heat transfer in multilayer structures:

```
program main
implicit none
external gval
integer N1,N2,j,ii,hmod,setup
real
x0,const1,const2,const3,A1(50,3),B1(50,3),d0micro,d0,d1micro,d1s,d1microf,d1f,d1,d,PI,time(100),timei
nit,timestep,i,m,fprobeMHz,fprobe,fmMHz,fm,K,Cp,t,fmax
real, allocatable :: A(:,:)
real, allocatable :: B(:,:)
complex simpson,delTr(100),delTi(100),partsumTr,partsumTi,parta,partb,delTTot(100)
parameter (PI=3.14159265358979323846)

! Open and read from parameter *.dat file
open (unit=1, file='parameter', status='old')

! First line in param file: fprobe(MHz),fmodulation(MHz),pump radius(micrometer),start probe
radius(micrometer),finish probe radius(micrometer)
read (1,*) fprobeMHz,fmMHz,d0micro,d1micro,d1microf
ii=1
t=0
! Side with metal layer that absorbs the heat
! Properties are input for top metal layer upto substrate (SS)
! Program recognizes SS by thickness=1
! Thermal conductivity(W/cm-K), volumetric sp heat(J/cm^3-K), thickness(m)
! Calculate material properties matrix B for the side that receives heat
do while (t.ne.1)
    N2=ii-1
    read (1,*) K,Cp,t
    B1(ii,1)=K*1.E2
    B1(ii,2)=(K/Cp)*1.E-4
    B1(ii,3)=t
    ii=ii+1
end do
ii=1
t=0
! Other side of the thermal system
! Calculate material properties matrix A for the other side
do while (t.ne.1)
    N1=ii-1
    ! If unidirectional HT model then skip calculating matrix A
    read (1,*,end=99) K,Cp,t

    A1(ii,1)=K*1.E2
    A1(ii,2)=(K/Cp)*1.E-4
    A1(ii,3)=t
    ii=ii+1
end do
```

```

99      continue
! Make sure to close the parameter file!!
close (unit=1)

allocate (A(N1+1,3))
allocate (B(N2+1,3))

! Actual matrix A and B of right sizes
A=A1(1:N1+1,1:3)
B=B1(1:N2+1,1:3)

!If ii=0 then unidirectional(hmod=1) else bidirectional(hmod=2) HT model
if (ii.eq.1) then
    hmod=1
else
    hmod=2
end if

!Create delay time array
! Negative delay times
j=1
do while (j.le.5)
    time(j)=-((200-40*(j-1))*1.E-12)
    j=j+1
end do

! Positive delay: Initial delay time, time step
timeinit=25.E-12
! End delay time ~ 3 ns
timestep=9.270607
! End delay time ~ 4.01 ns
!timestep=9.86
! Number of data points =60 (can be changed here)
do while (j.LE.60)
    time(j)=timeinit*(1+0.01*timestep)**(j-1-5)
    j=j+1
end do

fm=fmMHz*1.E6
fprobe=fprobeMHz*1.E6
d0=d0micro*1.E-6
d1s=d1micros*1.E-6
d1f=d1microf*1.E-6
! To account for changing probe beam radius
!  $w(x)^2 = w_0^2(1 + (\text{wavelength} * x / \pi * w_0^2)^2)^2 = w_0^2(1 + \text{Const} * x^2)^2$ 
!  $r = 1.27 * f * \text{wavelength} / w$ 
! x0 is the distance from focusing lens to objective lens when delay is set to minimum
x0=0.
!Calculate const
const3=(d1s/d1f)**2
const2=(const3-1)/((x0+3.e8*time(60))**2-const3*(x0**2))
const1=d1s*sqrt(1+const2*(x0**2))
!const=(d1s**2/d1f**2-1)/(1+time(60)*3.e8)**2

10 continue

```

```

print *, 'Delayed probe (1)/ Advanced pump setup (2):'
read *, setup
! Continue only if user inputs 1 or 2
if ((setup.eq.1) .or. (setup.eq.2)) then
    continue
else
    goto 10
end if
! Tell user to wait
print *, 'Wait...'

! Open file to write the data
open (unit=2,file='data',status='old')

j=1
do while (j.LE.60)
    !Calculate probe radius at given time t(j) and effective radius of overlpping beams d0

    if (j.le.5) then
        d1=d1s
    else
        !d1=d1s/sqrt(1+const*(1.+time(j)*3.e8)**2)
        d1=const1/sqrt(1+const2*((x0+3.e8*time(j)))**2)
    end if

    d=sqrt(d0**2+d1**2)

    delTr(j)=(0.,0.)
    delTi(j)=(0.,0)
    ! M=No of iterations, output converges for n=20 (We may use n=15 or 10 for faster run)
    M=abs(10/(fprobe*time(j)))
    i=0
    ! Maximum frequency considered in the calculation
    !fmax=10/abs(time(j))
    fmax=10/time(j)
    do while (i.LE.M)
        ! Calculate real and imaginary part of the signal
        if (i.eq.0) then
            parta=simpson(gval,2*pi*(fm),d,A,B,N1,N2,hmod,0.,2/d,20)
            partb=simpson(gval,(2*pi*(-fm)),d,A,B,N1,N2,hmod,0.,2/d,20)
            ! Multiplying with the Gaussian factor exp(-pi*((i*fprobe)/(fmax))**2)
            accelerates the convergence of real part of the signal
            partsumTr=2*PI*(parta+partb)*cexp(cmplx(0,2.*PI*i*fprobe*time(j)))*exp(-
            pi*((i*fprobe)/(fmax))**2)/2
            partsumTi=2*PI*(parta-partb)*cexp(cmplx(0,2.*PI*i*fprobe*time(j)))*exp(-
            pi*((i*fprobe)/(fmax))**2)/2
        else
            parta=simpson(gval,2*pi*(i*fprobe+fm),d,A,B,N1,N2,hmod,0.,2/d,20)
            partb=simpson(gval,2*pi*(i*fprobe-fm),d,A,B,N1,N2,hmod,0.,2/d,20)
            partsumTr=2*PI*(parta+partb)*cexp(cmplx(0,2.*PI*i*fprobe*time(j)))*exp(-
            pi*((i*fprobe)/(fmax))**2)
            partsumTi=2*PI*(parta-partb)*cexp(cmplx(0,2.*PI*i*fprobe*time(j)))*exp(-
            pi*((i*fprobe)/(fmax))**2)
        end if
        delTr(j)=delTr(j)+real(partsumTr)
    end do
    j=j+1
end do

```

```

        delTi(j)=delTi(j)+aimag(partsumTi)*cmplx(0,1)
        i=i+1
    end do
    ! Calculate complex total tempertaure
    if (setup.eq.1) then
        !Delayed probe case
        !delTtot(j)=delTr(j)+delTi(j)
        delTtot(j)=(real(delTr(j))+aimag(delTi(j))*cmplx(0,1))
    elseif (setup.eq.2) then
        !Advanced pump case
        !delTtot(j)=(delTr(j)+delTi(j))*cexp(cmplx(0,2*pi*fm*time(j)))
        delTtot(j)=(real(delTr(j))+aimag(delTi(j))*cmplx(0,1))*cexp(cmplx(0,2*pi*fm*time(j)))
    end if

    write (2,*) time(j),real(delTtot(j)),aimag(delTtot(j)),-real(delTtot(j))/aimag(delTtot(j))
    j=j+1.
end do
! EOF
end file (unit=2)
! Close the file
close (unit=2)
ii=1
do ii=1,25    ! Clear the screen
    print *
end do
end program main

```

```

!-----
! Simpson's rule: To calculate the integral
complex function simpson(gval,w,d,A,B,N1,N2,hmod,s,t,m)
implicit none
!external func
integer, INTENT(IN)::m,N1,N2,hmod
real, INTENT(IN):: w,d,A(N1+1,3),B(N2+1,3),s,t
real PI
integer i
parameter (PI=3.14159)
real h,z,deltaz
complex gval,sumodd,sumeve
h=(t-s)/m
deltaz=2.0*h
sumodd=0.0
z=s+h
do 10 i=2,m,2
    sumodd=sumodd+gval(w,z,d,A,B,N1,N2,hmod)
    z=z+deltaz
10    continue
sumeve=0.0
z=s+deltaz
do 20 i=2,m-2,2
    sumeve=sumeve+gval(w,z,d,A,B,N1,N2,hmod)
    z=z+deltaz
20    continue
simpson=(gval(w,z,d,A,B,N1,N2,hmod)+gval(w,z,d,A,B,N1,N2,hmod)+4*sumodd+2.0*sumeve)*(h/3.0)
return
end function simpson

```

```

!-----
!Function to evaluate gval=G
function gval(w,k,d,A,B,N1,N2,hmod)
implicit none
integer, INTENT(IN)::N1,N2,hmod
real, INTENT(IN)::w,k,A(N1+1,3),B(N2+1,3)
complex
g,gval,AA1(2,2),AA2(2,2),AA3(2,2),BA(2),CA(2,2),AB1(2,2),AB2(2,2),AB3(2,2),BB(2),CB(2,2),u1(N1+
1),gam1(N1+1),u2(N2+1),gam2(N2+1)
!real, INTENT(IN)::k
integer i
real d,PI,uLmax
parameter (PI=3.14159265358979323846,uLmax=10.)
!calculate u, gam for side with metal layer that receives all the heat (N2+1 layers)
call ugam(w,k,B,N2+1,u2,gam2)
! Decide G function(gval) model depending upon whether uni-D or bi-D heat model
! Matrix A computation
if (hmod.eq.1) then
    BA(1)=0.5
    BA(2)=0.5
else
    call ugam(w,k,A,N1+1,u1,gam1)
    if (N1.EQ.0) then
        ! Simpe case of one layer i.e. only SS on the other side
        BA(1)=(gam2(1)+gam1(1))/(2.*gam2(1))
        BA(2)=(gam2(1)-gam1(1))/(2.*gam2(1))
    else
        !calculate u, gam for the other side (N1+1 layers)
        CA(1,1)=(gam2(1)+gam1(1))/(2.*gam2(1))
        CA(1,2)=(gam2(1)-gam1(1))/(2.*gam2(1))
        CA(2,1)=(gam2(1)-gam1(1))/(2.*gam2(1))
        CA(2,2)=(gam2(1)+gam1(1))/(2.*gam2(1))

        do i=1,N1
            if (real(u1(i)*A(i,3)).LT.uLmax) then
                AA1(1,1)=cexp(u1(i)*A(i,3))
                AA1(1,2)=0.
                AA1(2,1)=0.
                AA1(2,2)=cexp(-u1(i)*A(i,3))
                AA2(1,1)=gam1(i)+gam1(i+1)
                AA2(1,2)=gam1(i)-gam1(i+1)
                AA2(2,1)=gam1(i)-gam1(i+1)
                AA2(2,2)=gam1(i)+gam1(i+1)
                call mat2x2prod(AA1,AA2,AA3)
                call mat2x2prod((1./(2.*gam1(i)))*CA,AA3,CA)

                !To fix FORTRAN compiler bug for real numbers >3e38
                if ((ABS(REAL(CA(1,1))).GE. 1.E35).OR.(abs(AIMAG(CA(1,1))).GE.
1.E35).or.(abs(REAL(CA(2,1))).GE. 1.E35).OR.(abs(AIMAG(CA(2,1))).GE. 1.E35)) THEN
                    CA=CA/1.e20
                end if

            if (i.EQ.N1) then

```

```

        BA(1)=CA(1,1)
        BA(2)=CA(2,1)
        goto 50
    end if
else
    !To fix FORTRAN compiler bug
for real numbers >3e38
    if ((ABS-REAL(CA(1,1))).GE. 1.E35).OR.(abs(AIMAG(CA(1,1))).GE.
1.E35).or.(abs-REAL(CA(2,1))).GE. 1.E35).OR.(abs(AIMAG(CA(2,1))).GE. 1.E35)) THEN
        CA=CA/1.e20
    end if

    !uLmax is large then simplify the matrix U
    BA(1)=CA(1,1)
    BA(2)=CA(2,1)
    goto 50
end if
end do
end if
50 continue

! Matrix B computation
CB(1,1)=1.
CB(1,2)=0.
CB(2,1)=0.
CB(2,2)=1.
if (N2.EQ.0) then
    BB(1)=0.
    BB(2)=1.
else
    do i=1,N2
        if (real(u2(i)*B(i,3)).LT.uLmax) then
            AB1(1,1)=cexp(-u2(i)*B(i,3))
            AB1(1,2)=0
            AB1(2,1)=0
            AB1(2,2)=cexp(u2(i)*B(i,3))
            AB2(1,1)=gam2(i)+gam2(i+1)
            AB2(1,2)=gam2(i)-gam2(i+1)
            AB2(2,1)=gam2(i)-gam2(i+1)
            AB2(2,2)=gam2(i)+gam2(i+1)
            call mat2x2prod(AB1,AB2,AB3)
            call mat2x2prod((1./(2.*gam2(i)))*CB,AB3,CB)

            !To fix FORTRAN compiler bug for real numbers >3e38
            if ((ABS-REAL(CB(1,2))).GE. 1.E35).OR.(abs(AIMAG(CB(1,2))).GE.
1.E35).or.(abs-REAL(CB(2,2))).GE. 1.E35).OR.(abs(AIMAG(CB(2,2))).GE. 1.E35)) THEN
                CB=CB/1.e20
            END IF

            if (i.EQ.N2) then
                BB(1)=CB(1,2)
                BB(2)=CB(2,2)
                ! Calculate G function
                g=(1/(2*gam2(1)))*(BB(1)+BB(2))*(BA(1)+BA(2))/(BA(1)*BB(2)-
BA(2)*BB(1))

```

```

                                gval=g*k*exp(-PI**2*k**2*d**2/2)
                                return
                                end if
else
    !To fix FORTRAN compiler bug for real numbers >3e38
    if ((ABS(REAL(CB(1,2))).GE. 1.E35).OR.(abs(AIMAG(CB(1,2))).GE.
1.E35).or.(abs(REAL(CB(2,2))).GE. 1.E35).OR.(abs(AIMAG(CB(2,2))).GE. 1.E35)) THEN
        CB=CB/1.e20
    end if

    !uLmax is large then simplify the matrix U
    BB(1)=CB(1,2)
    BB(2)=CB(2,2)
    ! Calculate G function
    g=(1/(2*gam2(1)))*(BB(1)+BB(2))*(BA(1)+BA(2))/(BA(1)*BB(2)-
BA(2)*BB(1))
    gval=g*k*exp(-PI**2*k**2*d**2/2)
    return
end if
end do
end if
end function gval

```

```

!-----
!Subroutine to evaluate u and gamma

```

```

subroutine ugam(w,k,A,N,u,gam)
implicit none
integer, INTENT(IN)::N
real, INTENT(IN)::w,k,A(N,3)
!real, INTENT(IN)::w,k,A(10,3)

real PI,i
complex q
complex, INTENT(OUT)::u(N),gam(N)
parameter(PI=3.14159265358979323846)
! Compute Q,U,GAM matrices
do i=1,N
    q=cmplx(0,w/A(I,2))
    u(i)=csqrt(4*PI**2*k**2+q)
    gam(i)=A(i,1)*u(i)
end do
end subroutine ugam

```

```

!-----
!Subroutine for multiplying two 2X2 matrices
subroutine mat2x2prod(A,B,C)
implicit none
complex, INTENT(IN)::A(2,2),B(2,2)
complex, INTENT(OUT)::C(2,2)
C(1,1)=A(1,1)*B(1,1)+A(1,2)*B(2,1)
C(1,2)=A(1,1)*B(1,2)+A(1,2)*B(2,2)
C(2,1)=A(2,1)*B(1,1)+A(2,2)*B(2,1)
C(2,2)=A(2,1)*B(1,2)+A(2,2)*B(2,2)
end subroutine mat2x2prod

```

```
!-----  
!Subroutine for multiplying two 2X2 matrices with one having multiplied by factor f  
subroutine mat2x2prodf(f,A,B,C)  
implicit none  
complex, INTENT(IN)::A(2,2),B(2,2)  
complex, INTENT(OUT)::C(2,2)  
complex f  
C(1,1)=f*(A(1,1)*B(1,1)+A(1,2)*B(2,1))  
C(1,2)=f*(A(1,1)*B(1,2)+A(1,2)*B(2,2))  
C(2,1)=f*(A(2,1)*B(1,1)+A(2,2)*B(2,1))  
C(2,2)=f*(A(2,1)*B(1,2)+A(2,2)*B(2,2))  
end subroutine mat2x2prodf  
  
!-----
```

Bibliography

1. Plawsky, J.L., *Transport Phenomena Fundamentals*. 2001, New York: Marcel Dekkar.
2. Carslaw, H.S. and J.C. Jaeger, *Conduction of Heat in Solids*. 1959, New York: Oxford University Press.
3. Berman, R., *Thermal Conduction in Solids*. 1976, Oxford: Oxford University Press.
4. Ozisik, M.N., *Heat Conduction*. 1980, New York: John Wiley & Sons.
5. Cahill, D.G., et al., *Nanoscale Thermal Transport*. *Journal of Applied Physics*, 2003. **93**(2): p. 793-818.
6. Cahill, D.G., K. Goodson, and A. Majumdar, *Thermometry and Thermal Transport in Micro/Nanoscale Solid-State Devices and Structures*. *Journal of Heat Transfer-Transactions of the Asme*, 2002. **124**(2): p. 223-241.
7. Cahill, D.G., *Heat Transport in Dielectric Thin Films and at Solid-Solid Interfaces*, in *Microscale Energy Transport*, C.L. Tien, A. Majumdar, and F.M. Gerner, Editors. 1997, Taylor & Francis: Washington D. C.
8. Yang, B. and G. Chen, *Experimental Studies on Thermal Conductivity of Thin Films and Superlattices*, in *Thermal Conductivity: Theory, Properties, and Applications*, T.M. Tritt, Editor. 2004, Kluwer Academic/ Plenum Publishers: New York. p. 167-186.
9. Lyeo, H.K. and D.G. Cahill, *Thermal Conductance of Interfaces between Highly Dissimilar Materials*. *Physical Review B*, 2006. **73**(14).

10. Ohring, M., *The Material Science of Thin Films*. 1992, San Diego: Academic Press.
11. Abramson, A.R., et al., *Fabrication and Characterization of a Nanowire/Polymer-Based Nanocomposite for a Prototype Thermoelectric Device*. *Journal of Microelectromechanical Systems*, 2004. **13**(3): p. 505-513.
12. Fan, X.F., et al., *Sigec/Si Superlattice Microcoolers*. *Applied Physics Letters*, 2001. **78**(11): p. 1580-1582.
13. Chen, G., et al., *Recent Developments in Thermoelectric Materials*. *International Materials Reviews*, 2003. **48**: p. 45-66.
14. Venkatasubramanian, R., et al., *Thin-Film Thermoelectric Devices with High Room-Temperature Figures of Merit*. *Nature*, 2001. **413**(6856): p. 597-602.
15. Rowe, D.M., *Crc Handbook of Thermoelectrics*. 1994, Boca Raton, FL: CRC press.
16. Shakouri, A. and J.E. Bowers, *Heterostructure Integrated Thermionic Coolers*. *Applied Physics Letters*, 1997. **71**(9): p. 1234-1236.
17. Mahan, G.D., *Thermionic Refrigeration*. *Recent Trends in Thermoelectric Materials Research Iii*, 2001. **71**: p. 157-174.
18. Mahan, G.D. and L.M. Woods, *Multilayer Thermionic Refrigeration*. *Physical Review Letters*, 1998. **80**(18): p. 4016-4019.
19. Chung, D.D.L., *Thermal Interface Materials*. *Journal of Materials Engineering and Performance*, 2001. **10**(1): p. 56-59.
20. Xu, J. and T.S. Fisher, *Enhanced Thermal Contact Conductance Using Carbon Nanotube Arrays*. *Itherm 2004, Vol 2*, 2004: p. 549-555.

21. Smith, A.N. and J.P. Calame, *Impact of Thin Film Thermophysical Properties on Thermal Management of Wide Bandgap Solid-State Transistors*. International Journal of Thermophysics, 2004. **25**(2): p. 409-422.
22. Biercuk, M.J., et al., *Carbon Nanotube Composites for Thermal Management*. Applied Physics Letters, 2002. **80**(15): p. 2767-2769.
23. Choi, S.U.S., et al., *Anomalous Thermal Conductivity Enhancement in Nanotube Suspensions*. Applied Physics Letters, 2001. **79**(14): p. 2252-2254.
24. Eastman, J.A., et al., *Thermal Transport in Nanofluids*. Annual Review of Materials Research, 2004. **34**: p. 219-246.
25. Padture, N.P., M. Gell, and E.H. Jordan, *Materials Science - Thermal Barrier Coatings for Gas-Turbine Engine Applications*. Science, 2002. **296**(5566): p. 280-284.
26. Hamad-Schifferli, K., et al., *Remote Electronic Control of DNA Hybridization through Inductive Coupling to an Attached Metal Nanocrystal Antenna*. Nature, 2002. **415**(6868): p. 152-155.
27. Huttmann, G. and R. Birngruber, *On the Possibility of High-Precision Photothermal Microeffects and the Measurement of Fast Thermal Denaturation of Proteins*. Ieee Journal of Selected Topics in Quantum Electronics, 1999. **5**(4): p. 954-962.
28. O'neal, D.P., et al., *Photo-Thermal Tumor Ablation in Mice Using near Infrared-Absorbing Nanoparticles*. Cancer Letters, 2004. **209**(2): p. 171-176.

29. West, J.L. and N.J. Halas, *Engineered Nanomaterials for Biophotonics Applications: Improving Sensing, Imaging, and Therapeutics*. Annual Review of Biomedical Engineering, 2003. **5**: p. 285-292.
30. Huxtable, S.T., et al., *Interfacial Heat Flow in Carbon Nanotube Suspensions*. Nature Materials, 2003. **2**(11): p. 731-734.
31. Ashcroft, N.W. and N.D. Mermin, *Solid State Physics*. 1976, Orlando, FL: W. B. Saunders.
32. Kittel, C., *Introduction to Solid State Physics*. 7th ed. 1996, New York: John Wiley.
33. Majumdar, A., *Microscale Energy Transport in Solids*, in *Microscale Energy Transport*, C.L. Tien, A. Majumdar, and F.M. Gerner, Editors. 1997, Taylor & Francis: Washington D.C.
34. Kurti, N., B.V. Rollin, and F. Simon, *Preliminary Experiments on Temperature Equilibria at Very Low Temperatures*. Physica, 1936. **3**(266).
35. Kapitza, P.L., *The Study of Heat Transfer in Helium II*. Journal of Physics (USSR), 1941. **4**(181).
36. Khalatnikov, I.M., *Teploobmen Mezhdru Tverdym Telom I Geliem-II*. ZHURNAL EKSPERIMENTALNOI I TEORETICHESKOI FIZIKI, 1952. **22**(687).
37. Swartz, E.T. and R.O. Pohl, *Thermal-Boundary Resistance*. Reviews of Modern Physics, 1989. **61**(3): p. 605-668.
38. Guan, W.-Y., *An Investigation of the Temperature Discontinuity at the Boundary Between a Solid and Superfluid Helium*. Zh. Eksp. Teor. Fiz., 1962. **42**(921).

39. Johnson, R.C. and W.A. Little, *Experiments on the Kapitza Resistance*. Physical Review, 1963. **130**(596).
40. Folinsbee, J.T. and A.C. Anderson, *The Kapitza Resistance to a Variety of Metallic Surfaces Below 0.3 K*. Journal of Low Temperature Physics, 1974. **17**(409).
41. Haug, H. and K. Weiss, *A Modified Theory of the Kapitza Resistance*. Physics Letters A, 1972. **45**(170).
42. Peterson, R.E. and A.C. Anderson, *The Kapitza Thermal Boundary Resistance*. Journal of Low Temperature Physics, 1973. **11**(639).
43. Little, W.A., *The Transport of Heat between Dissimilar Solids at Low Temperature*. Canadian Journal of Physics, 1959. **37**(334).
44. Swartz, E.T. and R.O. Pohl, *Thermal-Resistance at Interfaces*. Applied Physics Letters, 1987. **51**(26): p. 2200-2202.
45. Eisenmenger, W., *Phonon Scattering in Condensed Matter V*, in *Phonon Scattering at Surfaces and Interfaces* A.C. Anderson and J.P. Wolfe, Editors. 1986, Springer: Berlin/Heidelberg/New York. p. 204.
46. Snyder, N.S., *Heat Transport through Helium II: Kapitza Conductance*. Cryogenics, 1970. **10**(89).
47. Stoner, R.J. and H.J. Maris, *Kapitza Conductance and Heat-Flow between Solids at Temperatures from 50 to 300 K*. Physical Review B, 1993. **48**(22): p. 16373-16387.
48. Huberman, M.L. and A.W. Overhauser, *Electronic Kapitza Conductance at a Diamond-Pb Interface*. Physical Review B, 1994. **50**(5): p. 2865-2873.

49. Costescu, R.M., M.A. Wall, and D.G. Cahill, *Thermal Conductance of Epitaxial Interfaces*. Physical Review B, 2003. **67**(5).
50. Stevens, R.J., A.N. Smith, and P.M. Norris, *Measurement of Thermal Boundary Conductance of a Series of Metal-Dielectric Interfaces by the Transient Thermoreflectance Technique*. Journal of Heat Transfer-Transactions of the Asme, 2005. **127**(3): p. 315-322.
51. Gundrum, B.C., D.G. Cahill, and R.S. Averback, *Thermal Conductance of Metal-Metal Interfaces*. Physical Review B, 2005. **72**(24).
52. Mahan, G.D. and M. Bartkowiak, *Wiedemann-Franz Law at Boundaries*. Applied Physics Letters, 1999. **74**(7): p. 953-954.
53. Majumdar, A. and P. Reddy, *Role of Electron-Phonon Coupling in Thermal Conductance of Metal-Nonmetal Interfaces*. Applied Physics Letters, 2004. **84**(23): p. 4768-4770.
54. Kosevich, Y.A., *Fluctuation Subharmonic and Multiharmonic Phonon Transmission and Kapitza Conductance between Crystals with Very Different Vibrational-Spectra*. Physical Review B, 1995. **52**(2): p. 1017-1024.
55. Sergeev, A.V., *Electronic Kapitza Conductance Due to Inelastic Electron-Boundary Scattering*. Physical Review B, 1998. **58**(16): p. R10199-R10202.
56. Il'in, K.S., et al., *Interrelation of Resistivity and Inelastic Electron-Phonon Scattering Rate in Impure Nbc Films*. Physical Review B, 1998. **57**(24): p. 15623-15628.
57. Lee, S.M. and D.G. Cahill, *Heat Transport in Thin Dielectric Films*. Journal of Applied Physics, 1997. **81**(6): p. 2590-2595.

58. Li, B.C., et al., *Complete Thermal Characterization of Film-on-Substrate System by Modulated Thermoreflectance Microscopy and Multiparameter Fitting*. Journal of Applied Physics, 1999. **86**(9): p. 5314-5316.
59. Parrott, J.E. and S.A. D., *Thermal Conductivity of Solids*. 1975, London: Pion Limited.
60. Gustafsson, S.E. and E. Karawacki, *Transient Hot-Strip Probe for Measuring Thermal-Properties of Insulating Solids and Liquids*. Review of Scientific Instruments, 1983. **54**(6): p. 744-747.
61. Gustafsson, S.E., E. Karawacki, and M.N. Khan, *Transient Hot-Strip Method for Simultaneously Measuring Thermal-Conductivity and Thermal-Diffusivity of Solids and Fluids*. Journal of Physics D-Applied Physics, 1979. **12**(9): p. 1411-1421.
62. Cahill, D.G., *Thermal-Conductivity Measurement from 30-K to 750-K - the 3-Omega Method*. Review of Scientific Instruments, 1990. **61**(2): p. 802-808.
63. Cahill, D.G. [Http://Users.Mrl.Uiuc.Edu/Cahill/Tcdata/Tcdata.Html](http://Users.Mrl.Uiuc.Edu/Cahill/Tcdata/Tcdata.Html).
64. Paddock, C.A. and G.L. Eesley, *Transient Thermoreflectance from Thin Metal-Films*. Journal of Applied Physics, 1986. **60**(1): p. 285-290.
65. Kading, O.W., H. Skurk, and K.E. Goodson, *Thermal Conduction in Metallized Silicon-Dioxide Layers on Silicon*. Applied Physics Letters, 1994. **65**(13): p. 1629-1631.
66. Clemens, B.M., G.L. Eesley, and C.A. Paddock, *Time-Resolved Thermal Transport in Compositionally Modulated Metal-Films*. Physical Review B, 1988. **37**(3): p. 1085-1096.

67. Taketoshi, N., T. Baba, and A. Ono, *Observation of Heat Diffusion across Submicrometer Metal Thin Films Using a Picosecond Thermoreflectance Technique*. Japanese Journal of Applied Physics Part 2-Letters, 1999. **38**(11A): p. L1268-L1271.
68. Capinski, W.S., et al., *Thermal-Conductivity Measurements of GaAs/AlAs Superlattices Using a Picosecond Optical Pump-and-Probe Technique*. Physical Review B, 1999. **59**(12): p. 8105-8113.
69. Huxtable, S.T., D.G. Cahill, and L.M. Phinney, *Thermal Contact Conductance of Adhered Microcantilevers*. Journal of Applied Physics, 2004. **95**(4): p. 2102-2108.
70. Huxtable, S., et al., *Thermal Conductivity Imaging at Micrometre-Scale Resolution for Combinatorial Studies of Materials*. Nature Materials, 2004. **3**(5): p. 298-301.
71. Costescu, R.M., et al., *Ultra-Low Thermal Conductivity in W/Al₂O₃ Nanolaminates*. Science, 2004. **303**(5660): p. 989-990.
72. Cahill, D.G., *Analysis of Heat Flow in Layered Structures for Time-Domain Thermoreflectance*. Review of Scientific Instruments, 2004. **75**(12): p. 5119-5122.
73. Feldman, A., *Algorithm for Solutions of the Thermal Diffusion Equation in a Stratified Medium with a Modulated Heating Source*. High Temperatures-High Pressures, 1999. **31**(3): p. 293-298.
74. Kleiner, M.B., S.A. Kuhn, and W. Weber, *Thermal Conductivity Measurements of Thin Silicon Dioxide Films in Integrated Circuits*. Ieee Transactions on Electron Devices, 1996. **43**(9): p. 1602-1609.

75. Huxtable, S., et al., *Thermal Conductivity of Indium Phosphide Based Superlattices*, in *Thermoelectrics, 1999. Eighteenth International Conference On*. 1999: Baltimore, MD, USA. p. 594-597.
76. Cahill, D.G. and R.O. Pohl, *Thermal-Conductivity of Amorphous Solids above the Plateau*. *Physical Review B*, 1987. **35**(8): p. 4067-4073.
77. Incropera, F.P. and D.P. Dewitt, *Fundamentals of Heat and Mass Transfer*. 3rd ed. 1990, New York: John Wiley & Sons.
78. Website: http://en.wikipedia.org/wiki/Fused_Quartz.
79. Ogden, T.R., A.D. Rathsam, and J.T. Gilchrist, *Thermal-Conductivity of Thick Anodic Oxide Coatings on Aluminum*. *Materials Letters*, 1987. **5**(3): p. 84-87.
80. Webpage: <http://www.swiss-jewel.com/property.htm>.
81. Alexander, W. and J. Shackelford, *Crc Materials Science and Engineering Handbook*. Vol. 3. 2001, Boca Raton, FL: CRC Press.
82. Roukes, M.L., et al., *Hot-Electrons and Energy-Transport in Metals at Millikelvin Temperatures*. *Physical Review Letters*, 1985. **55**(4): p. 422-425.
83. Telford, M., *The Case for Bulk Metallic Glass*. *Materials Today*, 2004. **7**(3).
84. Byrne, C.J. and M. Eldrup, *Materials Science - Bulk Metallic Glasses*. *Science*, 2008. **321**(5888): p. 502-503.
85. Greer, A.L. and E. Ma, *Bulk Metallic Glasses: At the Cutting Edge of Metals Research*. *Mrs Bulletin*, 2007. **32**(8): p. 611-615.
86. Johnson, W.L., *Bulk Glass-Forming Metallic Alloys: Science and Technology*. *Mrs Bulletin*, 1999. **24**(10): p. 42-56.
87. Miller, M. and P.K. Liaw, *Bulk Metallic Glasses*. 2007, New York: Springer.

88. Morrison, M.L., et al., *Electrochemical Behavior of a Ti-Based Bulk Metallic Glass*. *Journal of Non-Crystalline Solids*, 2007. **353**(22-23): p. 2115-2124.
89. Inoue, A. and N. Nishiyama, *New Bulk Metallic Glasses for Applications as Magnetic-Sensing, Chemical, and Structural Materials*. *Mrs Bulletin*, 2007. **32**(8): p. 651-658.
90. Shanks, H.R., et al., *Thermal Conductivity of Silicon from 300 to 1400 K*. *Physical Review*, 1963. **130**(1743).
91. Lide, D.R., *Crc Handbook of Chemistry and Physics*. 82nd ed. 2002, Boca Raton, FL: Chemical Rubber Company.
92. Swamy, V., H.J. Seifert, and F. Aldinger, *Thermodynamic Properties of Y₂O₃ Phases and the Yttrium-Oxygen Phase Diagram*. *Journal of Alloys and Compounds*, 1998. **269**(1-2): p. 201-207.
93. Grahn, H.T., H.J. Maris, and J. Tauc, *Picosecond Ultrasonics*. *Ieee Journal of Quantum Electronics*, 1989. **25**(12): p. 2562-2569.
94. Palko, J.W., et al., *Elastic Constants of Yttria (Y₂O₃) Monocrystals to High Temperatures*. *Journal of Applied Physics*, 2001. **89**(12): p. 7791-7796.
95. Proust, C., et al., *Brillouin-Scattering in Cubic Phase of Yttrium Sesquioxide*. *Solid State Communications*, 1995. **93**(9): p. 729-732.
96. Klein, P.H. and W.H. Croft, *Thermal Conductivity, Diffusivity, and Expansion of Y₂O₃, Y₃Al₅O₁₂ and LaF₃ in the Range 77-300 K*. *Journal of Applied Physics*, 1967. **38**(1603).

97. Yamasaki, M., S. Kagao, and Y. Kawamura, *Thermal Diffusivity and Conductivity of Zr55al10ni5cu30 Bulk Metallic Glass*. Scripta Materialia, 2005. **53**(1): p. 63-67.
98. Yamasaki, M., et al., *Thermal Diffusivity and Conductivity of Supercooled Liquid in Zr41ti14cu12ni10be23 Metallic Glass*. Applied Physics Letters, 2004. **84**(23): p. 4653-4655.
99. Schroder, D.K., *Semiconductor Material and Device Characterization*. 2nd ed. 1998, New York: Wiley & Sons.
100. Einstein, A., *Elementary Observations on Thermal Molecular Motion in Solid Bodies*. Annalen der Physik, 1911. **35**(679).
101. Slack, G.A., *The Thermal Conductivity of Nonmetallic Crystals*, in *Solid State Physics*, H. Ehrenreich, F. Seitz, and D. Turnbull, Editors. 1979, Academic Press: New York. p. 1-71.
102. Cahill, D.G., S.K. Watson, and R.O. Pohl, *Lower Limit to the Thermal-Conductivity of Disordered Crystals*. Physical Review B, 1992. **46**(10): p. 6131-6140.
103. Birch, F. and H. Clark, *The Thermal Conductivity of Rocks and Its Dependence Upon Temperature and Composition*. American Journal of Science, 1940. **238**(529).
104. Kittel, C., *Interpretation of Thermal Conductivity of Glasses*. Physical Review, 1949. **75**(6): p. 972-974.
105. Cahill, D.G. and R.O. Pohl, *Heat-Flow and Lattice-Vibrations in Glasses*. Solid State Communications, 1989. **70**(10): p. 927-930.

106. Mashimo, T., et al., *Hugoniot-Compression Curve of Zr-Based Bulk Metallic Glass*. Applied Physics Letters, 2006. **89**(24): p. 3.
107. Koster, U. and L. Jastrow. *Oxidation of Zr-Based Metallic Glasses and Nanocrystalline Alloys*. in *12th International Conference on Rapidly Quenched and Metastable Materials*. 2005. Jeju Isl, SOUTH KOREA: Elsevier Science Sa.
108. Hammond, P.T., *Form and Function in Multilayer Assembly: New Applications at the Nanoscale*. Advanced Materials, 2004. **16**(15): p. 1271-1293.
109. Alivisatos, A.P., *Semiconductor Clusters, Nanocrystals, and Quantum Dots*. Science, 1996. **271**(5251): p. 933-937.
110. Balazs, A.C., T. Emrick, and T.P. Russell, *Nanoparticle Polymer Composites: Where Two Small Worlds Meet*. Science, 2006. **314**(5802): p. 1107-1110.
111. Decher, G., *Fuzzy Nanoassemblies: Toward Layered Polymeric Multicomposites*. Science, 1997. **277**(5330): p. 1232-1237.
112. Abiade, J.T., et al., *Structural and Magnetic Properties of Self-Assembled Nickel Nanoparticles in a Yttria Stabilized Zirconia Matrix*. Thin Solid Films, 2008. **516**(8): p. 2082-2086.
113. Abiade, J.T., et al., *The Effect of Matrix and Substrate on the Coercivity and Blocking Temperature of Self-Assembled Ni Nanoparticles*. Journal of Applied Physics, 2008. **104**(7).
114. Tojo, T., et al., *Excess Heat Capacity in Yttria Stabilized Zirconia*. Journal of Thermal Analysis and Calorimetry, 1999. **57**(2): p. 447-458.

115. Schlichting, K.W., N.P. Padture, and P.G. Klemens, *Thermal Conductivity of Dense and Porous Ytria-Stabilized Zirconia*. Journal of Materials Science, 2001. **36**(12): p. 3003-3010.
116. Hasselman, D.P.H., et al., *Thermal-Diffusivity and Conductivity of Dense Polycrystalline Zro2 Ceramics - a Survey*. American Ceramic Society Bulletin, 1987. **66**(5): p. 799-806.
117. Hasselman, D.P.H. and L.F. Johnson, *Effective Thermal-Conductivity of Composites with Interfacial Thermal Barrier Resistance*. Journal of Composite Materials, 1987. **21**(6): p. 508-515.
118. Bruggeman, D.A.G., *Calculation of Various Physics Constants in Heterogenous Substances I Dielectricity Constants and Conductivity of Mixed Bodies from Isotropic Substances*. Ann. Phys., 1935. **24**(636).
119. Every, A.G., et al., *The Effect of Particle-Size on the Thermal-Conductivity of Zns Diamond Composites*. Acta Metallurgica Et Materialia, 1992. **40**(1): p. 123-129.
120. Yuan, S.P. and P.X. Jiang, *Thermal Conductivity of Small Nickel Particles*. International Journal of Thermophysics, 2006. **27**(2): p. 581-595.
121. Yakabe, H., et al., *Evaluation of Residual Stresses in a Sofc Stack*. Journal of Power Sources, 2004. **131**(1-2): p. 278-284.
122. Neighbours, J.R., F.W. Bratten, and C.S. Smith, *The Elastic Constants of Nickel*. Journal of Applied Physics, 1952. **23**(4).